

NASA Contractor Report 198482  
UCICL-ARTR-93-4

# Optimization of Orifice Geometry for Cross-Flow Mixing in a Cylindrical Duct

J.T. Kroll, W.A. Sowa, and G.S. Samuelsen  
*University of California*  
*Irvine, California*

April 1996

Prepared for  
Lewis Research Center  
Under Grant NAG3-1110



National Aeronautics and  
Space Administration



## TABLE OF CONTENTS

LIST OF TABLES .....	iv
LIST OF FIGURES .....	v
LIST OF SYMBOLS .....	vii
ABSTRACT .....	viii
CHAPTER 1: INTRODUCTION.....	1
1.1 Overview.....	1
1.2 Research Goals and Objectives.....	3
CHAPTER 2: BACKGROUND.....	4
2.1 HSCT Initiative.....	4
2.2 Oxides of Nitrogen Emissions.....	5
2.3 Low NO <sub>x</sub> Combustor Concepts.....	7
2.4 Mixing of Jets in a Cross Flow .....	11
CHAPTER 3: APPROACH.....	14
CHAPTER: 4 EXPERIMENT.....	17
4.1 Facility .....	17
4.1.1 Flow Panel .....	17
4.1.2 Test Stand .....	17
4.2 Diagnostics .....	20
4.2.1 Thermocouple Probe Design .....	21
4.2.2 Data Resolution between Measurement Planes .....	25
4.2.3 Data Resolution between Measurement Points .....	27
4.3 Test Matrix Specification .....	29
4.3.1 Jet Penetration as a Function of Orifice Design .....	31
4.3.2 Circular Orifice Optimization.....	31

4.3.3 Global Orifice Optimization .....	32
4.4 Execution of Experiments.....	32
4.5 Analysis .....	34
CHAPTER 5: RESULTS AND DISCUSSION.....	36
5.1 Jet Penetration as a Function of Orifice Design .....	36
5.2 Circular Orifice Optimization.....	41
5.2.1 Mixing Downstream of the Orifice.....	42
5.2.2 Mixing at One Duct Radius Downstream.....	47
5.3 Global Orifice Optimization .....	50
5.3.1 Mixture Fraction Contours at $z/R=1.0$ .....	52
5.3.2 Linear Regression Analysis .....	61
CHAPTER 6: CONCLUSIONS AND RECOMMENDATIONS .....	63
6.1 Conclusions.....	63
6.2 Recommendations.....	64
CHAPTER 7: REFERENCES.....	65
APPENDIX A: DERIVATION .....	68

## LIST OF TABLES

Table 4.1 Box Behnken Test Matrix .....	33
Table 5.1 Normalized Circular Orifice Axial Height and Percent Blockage .....	42
Table 5.2 Circular Orifice Operating Conditions .....	42
Table 5.3 Semi-Quantitative Jet Trajectory Characteristics For J=73 Round Hole Modules .....	47
Table 5.4 Normalized Orifice Axial Height and Percent Blockage .....	51
Table 5.5 Global Optimization Operating Conditions .....	51
Table 5.6 Average Mixture Fraction STD values at $z/R=1.0$ .....	59
Table 6.1 Additional Global Optimization Experiments .....	64

## LIST OF FIGURES

Figure 1.1 Schematic of a Gas Turbine Combustor.....	1
Figure 2.1 Schematic of a Conventional Gas Turbine Annular Combustor .....	8
Figure 2.2 Schematic of a Lean-Premixed-Prevaporized Combustor .....	8
Figure 2.3 Schematic of a Lean Burn Direct Injected Combustor .....	9
Figure 2.4 Schematic of a Rich Burn-Quick Mix-Lean Burn Combustor .....	10
Figure 4.1 Flow Panel Schematic .....	18
Figure 4.2 Test Stand Schematic .....	19
Figure 4.3 Test Assembly .....	20
Figure 4.4 Mixing Module Dimensions.....	20
Figure 4.5 Straight Axial-Aligned Probe .....	22
Figure 4.6 Effect of Variations in Thermocouple Probe Orientation on Mixture Fraction for 12 Circular Orifice J=36 Module.....	24
Figure 4.7 Orifice Plane Terminology .....	25
Figure 4.8 Effect of Variations in Thermocouple Probe Orientation on Mixture Fraction for 8 Circular Orifice J=73 Module.....	26
Figure 4.9 Measurement Planes.....	27
Figure 4.10 Eight Orifice Module Data Sectors for Single and Dual Orifice Mapping.....	28
Figure 4.11 Planar Data Point Grid of Sparse Density .....	30
Figure 4.12 Planar Data Point Grid of Intermediate Density.....	30
Figure 4.13 Final Planar Data Point Grid Density.....	31
Figure 4.14 Graphical Illustration of Box-Behnken Test Matrix .....	33
Figure 5.1 Center Line Mixture Fraction Measurements for Round Hole Modules.....	37

Figure 5.2 Center Line Mixture Fraction Measurements for 4:1 AR @ 45 Degrees	
Modules.....	38
Figure 5.3 Center Line Mixture Fraction Measurements for 8:1 AR @ 45 Degrees	
Modules.....	39
Figure 5.4 Local Mixture Fraction Contours for the J=73 Modules.....	44
Figure 5.5 Local Mixture Fraction Contours for the J=36 Modules.....	45
Figure 5.6 Example of Jet Trajectory Features Characterized.....	46
Figure 5.7 Area Weighted Standard Deviation Per Plane for the J=73 Momentum	
Flux Ratio Modules .....	48
Figure 5.8 Area weighted Standard Deviation Per Plane for the J=36 Momentum	
Flux Ratio Modules .....	49
Figure 5.9 Area Weighted Standard Deviation as a Function of the Number of	
Orifices at @ $z/R=1.0$ .....	49
Figure 5.10 Mean Jet Trajectory Penetration Depth @ $z/R=1.0$ for the J=73	
Momentum Flux Ratio Modules.....	50
Figure 5.11 Graphical Representation of Test Matrix .....	53
Figure 5.12 Sixteen Orifice Modules' Design Plane .....	55
Figure 5.13 Sixteen Orifice Modules' Mixture Fraction Contours at $z/R=1.0$ .....	55
Figure 5.14 Twelve Orifice Modules' Design Plane .....	57
Figure 5.15 Twelve Orifice Modules' Mixture Fraction Contours at $z/R=1.0$ .....	57
Figure 5.16 Eight Orifice Modules' Design Plane.....	58
Figure 5.17 Eight Orifice Modules' Mixture Fraction Contours at $z/R=1.0$ .....	58
Figure 5.18 STD Results as a Function of the Orifice Design Parameters at	
$z/R=1.0$ .....	59
Figure 5.19 Mean Jet Penetration Results at $z/R=1.0$ as a Function of the Orifice	
Design Parameters.....	60

## LIST OF SYMBOLS

AR	aspect ratio
d	jet orifice diameter
DR	jet-to-mainstream density ratio
$f$	mixture fraction
h	orifice axial height projection
h/R	normalized orifice axial height projection
J	jet-to-mainstream momentum-flux ratio
MR	jet-to-mainstream mass-flow ratio
R	mixer radius, 1.5 inches
STD	mixture fraction standard deviation
z	axial distance, zero at orifice leading edge
z/R	normalized axial distance downstream of the leading edge of the orifice
z/d	normalized axial distance downstream of the leading edge of the orifice



## ABSTRACT

Mixing of gaseous jets in a cross-flow has significant applications in engineering, one example of which is the dilution zone of a gas turbine combustor. Despite years of study, the design of jet injection in combustors is largely based on practical experience. The emergence of  $\text{NO}_x$  regulations for stationary gas turbines and the anticipation of aero-engine regulations requires an improved understanding of jet mixing as new combustor concepts are introduced. For example, the success of the staged combustor to reduce the emission of  $\text{NO}_x$  is almost entirely dependent upon the rapid and complete dilution of the rich zone products within the mixing section. It is these mixing challenges to which the present study is directed. A series of experiments was undertaken to delineate the optimal mixer orifice geometry. A cross-flow to core-flow momentum-flux ratio of 40 and a mass flow ratio of 2.5 were selected as representative of a conventional design. An experimental test matrix was designed around three variables: the number of orifices, the orifice length-to-width ratio, and the orifice angle. A regression analysis was performed on the data to arrive at an interpolating equation that predicted the mixing performance of orifice geometry combinations within the range of the test matrix parameters. Results indicate that the best mixing orifice geometry tested involves eight orifices with a long-to-short side aspect ratio of 3.5 at a twenty-three degree inclination from the center-line of the mixing section.



## CHAPTER 1

### INTRODUCTION

#### 1.1 Overview

Jets in a cross flow constitute a flow arrangement that is integral to a number of areas important in combustion and energy science and technology.

In a gas turbine combustor for example (Figure 1.1), mixing of relatively cold air jets can significantly affect both combustor efficiency and emissions. Jets in a subsonic cross flow are also encountered in other airborne and terrestrial combustion applications, such as in premixing of fuel and air. In addition, mixing of transverse jets is important in applications such as the discharge of effluent in water, and in transition from hover to cruise for short take-off and vertical landing (STOVL) aircraft.

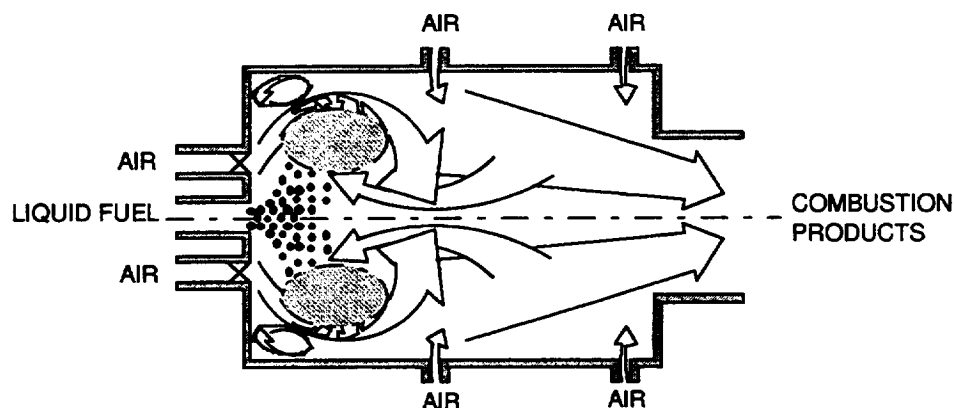


Figure 1.1 Schematic of a gas turbine combustor.

Gas turbines are used in a variety of applications due to their high power-to-weight ratio and their ability to rapidly transition from start-up to full load status. Stationary power generation installations take advantage of the quick start-up characteristics of gas turbines by utilizing them to augment base load generators during periods of peak electricity use. The high power-to-weight ratio of the gas turbine engine has enabled it to

serve with distinction as the propulsion units for military, commercial and private aircraft. Other examples of its use as a propulsion device include marine craft and locomotives, with potential uses in automobiles, buses and trucks.

In all these cases, the emission of  $\text{NO}_x$  is becoming the dominant challenge. For example, in fiscal year 1990, NASA initiated a six year program aimed at addressing the key technological barriers that challenge the development of a fleet of High Speed Civil Transport (HSCT) aircraft. These supersonic, air-breathing transports will fly in the stratosphere to reduce drag in an effort to remain economically feasible. Initial atmospheric model predictions suggest that unusually low  $\text{NO}_x$  emissions will be required to minimize the impact on the ozone layer (Johnston, 1971).

The Emissions Index (EI) is a value that is used to quantify the relative level of  $\text{NO}_x$  emissions for a given engine. The EI is defined as the number of grams of  $\text{NO}_x$  produced per kilogram of fuel burned. The EI of the Concorde's Olympus engine is approximately 20 (Shaw 1991). The combustion temperatures and pressures of an HSCT will be higher than those experienced by the Concorde. Shaw extrapolated current engine technology to HSCT conditions and obtained an EI in the range of 30 to 80. He concluded that a reduction of  $\text{NO}_x$  emissions of approximately 90% will be required to reach the NASA High Speed Research (HSR) goal of EI's in the range of 3 to 8 at supersonic cruise operating conditions.

The key to reducing the  $\text{NO}_x$  emissions to an acceptable level is to avoid the high reaction temperatures and associated high levels of  $\text{NO}_x$  production by performing the combustion process at off-stoichiometric conditions. One concept being investigated is the Rich Burn-Quick Mix-Lean Burn (RQL) combustor. The RQL combustor involves a staged burner concept where the first stage is fuel rich and the second is fuel lean. The transition from the rich zone to the lean zone is accomplished via the rapid introduction of quench air. The rapid and complete dilution of the rich zone products within the quick mix section is essential to the success of the RQL combustor.

The present study addresses the fundamental mixing characteristics that govern the optimal mixing in cylindrical ducts.

## **1.2 Research Goals and Objectives**

The goals of the present study are to (1) establish criteria for the selection of an optimal mixer, and (2) identify the optimal mixing configuration. To achieve these goals, the following objectives have been established:

1. Evaluate the effect of utilizing an intrusive probe for measurements within a subsonic flow field.
2. Select a probe which minimizes the flow field perturbations.
3. Design a test matrix that will facilitate a regression analysis to reveal the optimal mixing configuration.
4. Design and fabricate the mixers that are identified within the test matrix.
5. Conduct the experiments and perform a regression analysis.

## **CHAPTER 2**

### **BACKGROUND**

#### **2.1 HSCT Initiative**

In 1986, NASA initiated a multi-year research program aimed at determining whether a High Speed Civil Transport (HSCT) is economically possible and environmentally acceptable (Ott, 1988).

In 1988, Strack reported that although the Concorde pioneered the supersonic transport era, it has been commercially unsuccessful for a number of reasons. One reason is due to the fuel inefficiencies of the aircraft. The Concorde consumes about three times as much fuel per seat-mile as equivalent technology for subsonic long-range aircraft. The primary cause of the Concorde's high fuel consumption is the dramatic fall in the aircraft's lift-to-drag ratio at supersonic speeds; on the order of one-half that of subsonic transports. Current and future technology advances are estimated to provide efficiency gains of 40 percent or more over the Concorde's Olympus engines. The conclusion to be drawn from this analysis is that the large HSCT fuel consumption impediment can be overcome, but it will require very large technology gains in all disciplines -- propulsion, airplane aerodynamics, and airframe structures.

The HSR program is founded on the scenario of developing a fleet of aircraft with a 250-300 person capacity, a 5,500-6,500 nautical mile range, and the capability to cruise in the stratosphere at Mach 2-3 (Kandebo, 1989). The manufactures' hope to develop a fleet of 500-1,000 aircraft (Ott, 1988).

The objective of the HSR research program is to determine whether a high-speed transport is economically possible and environmentally acceptable. Phase 1 of the HSR project began in Fiscal 1990 and will run through Fiscal 1995. This phase of the HSR program will focus on addressing the technological feasibility of such an aircraft, with emphasis on ozone layer depletion as a result of NO<sub>x</sub> emissions in the stratosphere

(Kandebo, 1989). Phase 2 could begin in Fiscal 1994 and conclude in Fiscal 2001 to support an HSCT that could enter service in 2005 (Kandebo, 1992).

Strack and Morris (1988) identified low emissions combustion systems as one of the major challenges facing the propulsion community for viable civil supersonic transport development.

## **2.2 Oxides of Nitrogen Emissions**

Peters and Hammond (1990) classify combustion pollutants as either products of incomplete combustion (e.g., soot and carbon monoxide) or products of excessive oxidation of otherwise neutral species (e.g., oxides of nitrogen). Incomplete combustion products are controlled by completing the oxidation process, while products of excessive oxidation must be controlled by inhibiting their formation.

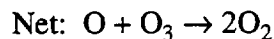
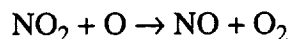
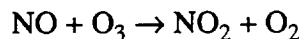
Two general areas of concern in regard to gas turbine emissions are addressed by Lefebvre (1983): (1) urban air pollution in the vicinity of airports and (2) pollution of the stratosphere. The main pollutants currently thought to be important are smoke, carbon monoxide (CO), unburned hydrocarbons (UHC), sulfur oxides (SO<sub>x</sub>), and oxides of nitrogen (NO<sub>x</sub>). The pollutant scenario of greatest concern to the HSR program is NO<sub>x</sub> emissions in the stratosphere.

This concern stems from the public awareness of the link between NO<sub>x</sub> emissions and stratospheric ozone (O<sub>3</sub>) depletion. In 1971, Johnston sounded an alarm concerning the potential for stratospheric ozone depletion from the exhaust emissions of supersonic transport (SST) aircraft that NASA was considering at the time. The estimated residence half-life of 1 to 5 years for pollutants of any type in the earth's stratosphere is of great concern. This remarkable time lag between the entrance and exit of species is due to the stratosphere's temperature inversion which provides stability against vertical mixing.

Johnston considered thirty-one chemical reactions in his modeling efforts of the effect of SST exhaust emissions on the stratosphere. Many of the reactions fixed the relative concentrations of O with respect to O<sub>3</sub>, of HO with respect of HOO, and of NO

with respect to  $\text{NO}_2$ . A few of the reactions had the effect of changing the concentration of oxygen molecules. These are the most important reactions with respect to ozone.

The combined effect of the following two reactions acts as a catalytic cycle.



Ozone is depleted in the first reaction, while NO is reconstituted in the second reaction. The result is a depletion in ozone concentration with no net change in either NO or  $\text{NO}_2$  concentrations. The catalytic cycle can be repeated indefinitely, allowing one mole of  $\text{NO}_x$  to destroy several moles of  $\text{O}_3$ .

Under normal gas turbine operating conditions, particularly at high emission levels, 95% of the total  $\text{NO}_x$  emitted is in the form of NO (Fletcher, 1980). For that reason, the mechanisms for the production of NO are of greatest concern when attempting to minimize  $\text{NO}_x$  emissions.

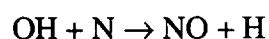
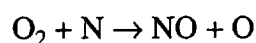
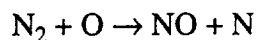
Nitric oxide can be produced by three different mechanisms. These mechanisms are commonly known by the names of fuel, prompt, and thermal. Fuel NO is produced by the oxidation of the fuel bound nitrogen. Fletcher (1980) reports that the conversion of fuel-bound nitrogen to NO is approximately 100% for fuel lean flames operating at low nitrogen concentrations (less than 0.5% by weight). However, for highly refined petroleum products such as jet fuels, fuel NO is negligible.

The two main mechanisms by which nitric oxide can be formed from atmospheric nitrogen are prompt and thermal. The discovery of the prompt NO mechanism arose due to the discrepancy between measured and calculated NO values. Prompt NO forms quickly at the flame front by the attack of hydrocarbon radicals on diatomic nitrogen. The exact chemistry is not fully understood, but appears to be linked to the interactions



between the many intermediary species that are produced during the main HC-CO-CO<sub>2</sub> reactions (Fletcher, 1980).

Thermal NO, the most important of the three mechanisms, involves the direct reaction of nitrogen with oxygen. Its kinetics are well understood and proceed according to the “extended” Zeldovich mechanism (1946) given below.



The chain is initiated by an oxygen radical from the dissociation of unburned oxygen molecules. The oxygen radical reacts with a nitrogen molecule to form NO and N. Equilibrium dissociation of nitrogen molecules is not achieved at the temperatures encountered in conventional turbine combustor, making the only source of N atoms the first reaction (Lefebvre, 1983). The first reaction is the rate-limiting reaction, proceeding at a significant rate only at temperatures above approximately 1800 K (2780 °F).

Lefebvre (1983) writes that for most practical purposes, it is sufficient to regard all other combustor parameters as significant only insofar as they affect flame temperature. As such, the primary goal when attempting to reduce NO<sub>x</sub> must be to lower the reaction temperature.

### 2.3 Low NO<sub>x</sub> Combustor Concepts

A schematic of the cross-section of a conventional gas turbine annular combustor is shown in Figure 2.1. High temperature and high pressure air enter the combustor from the left through the diffuser. The primary zone is run fuel-rich to maintain a stable flame. Air is introduced through the primary dilution holes to reduce the combustor's equivalence ratio to a fuel-lean fuel/air ratio. The combustion process is completed within the intermediate zone. The dilution zone is used to cool the exhaust products down to an acceptable level for the turbine blades.

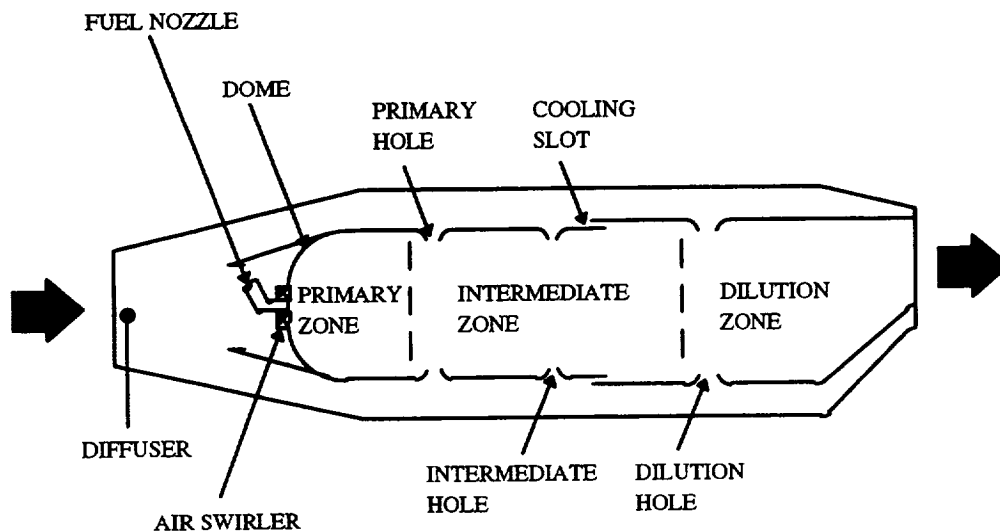


Figure 2.1 Schematic of a conventional gas turbine annular combustor

The LPP concept, shown in Figure 2.2, is rather simple in design. It involves providing a uniform mixture of fuel vapor and air to the main air stream, which burns at low temperatures where  $\text{NO}_x$  production is minimal. The disadvantage of the design is its narrow stability limits and its propensity for auto ignition and flashback.

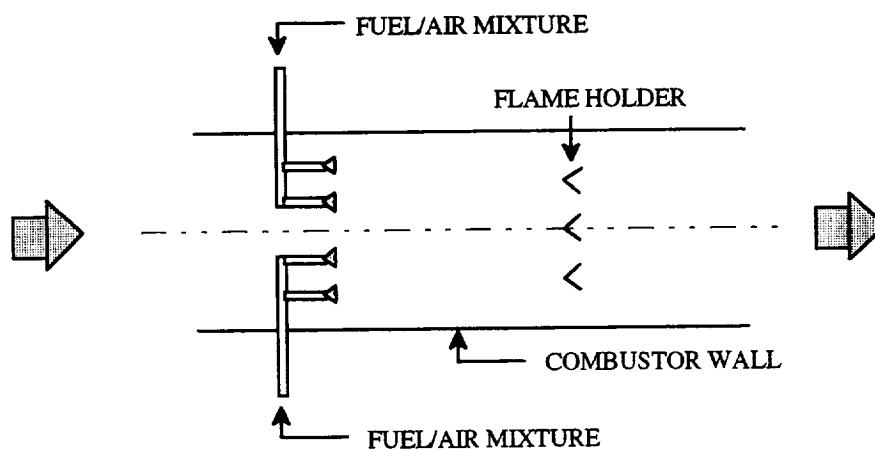


Figure 2.2 Schematic of a Lean-Premixed-Prevaporized (LPP) combustor (Adapted from Hatch et al., 1994)

The LDI concept is shown in Figure 2.3. This combustor is based on a simple design as well. The fuel is injected directly into the combustion zone. The success of this concept relies heavily upon quick vaporization of the liquid spray, and rapid and

uniform mixing of the fuel and air to avoid packets of stoichiometric regions where  $\text{NO}_x$  would be great.

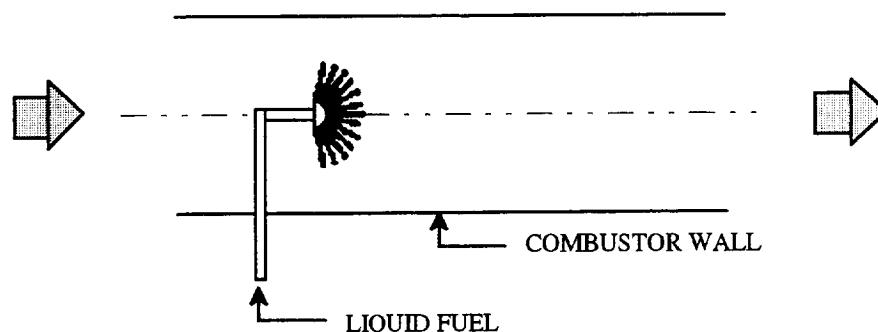


Figure 2.3 Schematic of a Lean Burn Direct Injected (LDI) combustor (Adapted from Hatch et al., 1994)

The RQL combustor was originally investigated in the 1970's as a means of minimizing  $\text{NO}_x$  production from burning fuels with high nitrogen contents (Mosier et al., 1980). In a lean burn system, nearly 100% of the fuel-bound nitrogen is converted into  $\text{NO}_x$ , whereas very little of the fuel-bound nitrogen is converted to  $\text{NO}_x$  in a rich flame (Tacina 1990). The RQL concept is the most complex of the three low  $\text{NO}_x$  designs considered here. Shown in Figure 2.4, the RQL combustor involves a staged approach to combustion. The combustion process is initiated in a fuel rich zone where the flame temperature is low. The quick mix section is designed to rapidly dilute the rich zone products before the combustion process is completed within the lean zone where again the flame temperature is low and thermal  $\text{NO}_x$  production is kept to a minimum. Rizk and Mongia (1990) mention two functions of the reduced diameter of the mixer: (1) it forces the rich zone products to accelerate into the mixer, thereby inhibiting any upstream mixing, and (2) it provides an expansion into the lean zone which initiates a stable combustion region. An advantage offered by the RQL combustor is that it possesses the stability characteristics of a conventional combustor due to its rich front end. The disadvantage is that in the mixing section where the rich zone products are

being diluted down with the addition of the jet air to an overall lean stoichiometry, the mixture must pass through the stoichiometric equivalence ratio where flame temperature and the thermal  $\text{NO}_x$  are high.

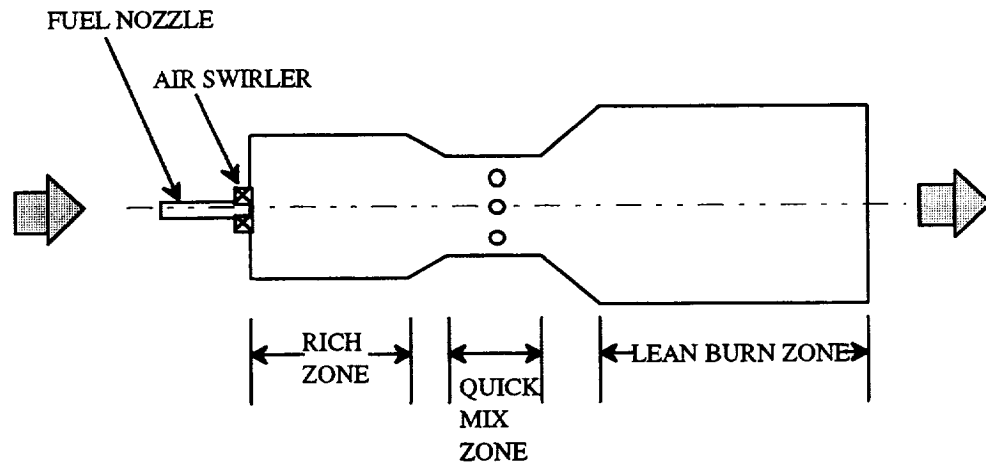


Figure 2.4 Schematic of a Rich Burn-Quick Mix-Lean Burn (RQL) combustor

Nakata et al. (1992) developed and tested an RQL combustor for achieving low fuel- $\text{NO}_x$  combustion of coal gasified fuel containing ammonia ( $\text{NH}_3$ ). The principal combustible components of the coal derived gaseous fuel produced in the coal gasifiers are carbon monoxide ( $\text{CO}$ ) and hydrogen ( $\text{H}_2$ ). Inert gases such as nitrogen ( $\text{N}_2$ ) and carbon dioxide ( $\text{CO}_2$ ) account for over 70 percent of the fuel composition. Additionally, hot gas cleaning systems pass significant quantities of ammonia on the combustor. The ammonia, a form of fuel bound nitrogen, would be converted to  $\text{NO}_x$  in a conventional combustor.

Their staged combustor consisted of three main sections; an auxiliary chamber, a primary chamber, and a secondary chamber. Fifteen percent of the total fuel input was burned in the auxiliary chamber to maintain a stoichiometric pilot flame for the primary chamber. Under the primary zone conditions, the fuel bound ammonia was decomposed to nitrogen in a reducing flame. The remaining components of the fuel are burned in the lean secondary chamber.

Thermal  $\text{NO}_x$  production was rather insignificant (approximately 3 ppm corrected to 16%  $\text{O}_2$ ) due to the low flame temperature resulting from the low heating value and the high percentage of inert gases in the fuel. The maximum gas temperature at the combustor exit was 1300 °C.

The advanced combustor achieved improved combustion stability and successfully reduced the  $\text{NO}_x$  emissions by more than half. While this example demonstrates the potential for the RQL combustor, its adaptation to the gas turbine combustor with higher inlet air temperatures, higher fuel heating value, and resulting higher flame temperatures, will be more difficult to successfully implement.

Tacina (1990) performed a literature review of both experimental and computational low  $\text{NO}_x$  combustor programs. He compared the relative emissions performance of the Lean-Premixed-Prevaporized (LPP) combustor, the Lean Burn Direct Injected (LDI) combustor, and the Rich Burn-Quick Mix-Lean Burn (RQL) combustor.

Although the RQL's combustor had higher levels of  $\text{NO}_x$  than the LPP or LDI combustors, Tacina attributed the problem to the gases in the RQL combustor spending time at near stoichiometric conditions in the quick mix section. Tacina felt that an optimized mixer design could reduce the overall RQL  $\text{NO}_x$  levels to within the levels of the other two designs.

This study addresses the mixing processes that occur in the quick mix section. The next section addresses the previous studies relevant to this application.

## **2.4 Mixing of Jets in a Cross Flow**

In Hatch et al. (1992), the mixing characteristics of both circular and slanted slot jet orifices in a cylindrical duct were studied, where the number of orifices for each mixer was held constant at eight. Mixing performance was observed to be strongly dependent on momentum-flux ratio as well as orifice design. Moreover, the need to consider configurations with more than eight orifices was evident. At a jet-to-mainstream momentum-flux ratio of 25, it appeared that the eight orifice round hole module had near

optimal penetration, whereas the slanted slot modules showed severe under penetration of the jet air. While a comparison between un-optimized orifice geometries provides a basic understanding of the different mixing mechanisms at work, it is necessary to compare optimized geometries in order to select one orifice design over the other.

The majority of the previous research on jets-in-a-confined-crossflow has been performed in rectangular geometries with the primary influence being jet mixing in annular combustors. The influence of orifice geometry and spacing, jet-to-mainstream momentum-flux ratio ( $J$ ), and density ratio ( $DR$ ) has been summarized for single and double sided injection by Holdeman (1993). • More recent studies of jets in a confined crossflow in a rectangular duct have been reported by Smith (1990), Liscinsky et al. (1992 and 1993), and Bain et al. (1992 and 1993).

As a result of these studies, momentum-flux ratio, orifice geometry, and orifice spacing have been identified as dominant parameters influencing the mixing. These observations are supported by the findings of Hatch et al. (1992) who observed that, even though eight circular orifices at a momentum-flux ratio ( $J$ ) of 25 provide optimum mixing, eight circular jets at  $J=80$  over-penetrate and impinge upon one another at the module's center line resulting in deteriorated mixing. Further support to the theory of an optimum number of orifices at a given momentum-flux ratio is provided by Liscinsky et al. (1992).

Analyses and experiments of jet mixing in a can configuration have been reported by Bruce et al. (1979). Among the results therein, is the hypothesis that the effective orifice spacing is that at half the radius of the can. A computational study reported by Holdeman et al. (1991) suggested that results for a rectangular duct and a can were similar if the orifice spacing for the latter were specified at the radius that divides the can into equal areas. Recent experimental and computational studies in a cylindrical geometry are reported in Talpallikar et al. (1991), Smith et al. (1991), Vranos et al. (1991), and Oechsle et al. (1992).

A computational study of mixing was conducted by Oechsle et al. (1992) for square, elongated slot, and equilateral triangle orifice configurations. The study concluded that mixing can be detrimentally effected by either under or over penetrating jets. Under penetrating jets allowed an undiluted core of main flow to pass through the mixing section. Similarly, over penetrating jets provide the opportunity for pure main flow to escape along the walls of the mixing section.

The proceeding studies have identified the important jet mixing design parameters as: jet-to-mainstream momentum-flux ratio, orifice geometry, orifice spacing, and the jet penetration depth. The present study seeks to identify the optimum combination of these parameters. As a first step, the four parameters can be simplified when the orifice spacing is considered as a function of the orifice geometry. Likewise, for a given momentum-flux ratio, jet penetration is also a function of the orifice geometry. Therefore, to optimize the mixing of jets into a cross-flow in a can configuration, the important design parameters can be reduced to the jet-to-mainstream momentum-flux ratio and the orifice geometry.

## CHAPTER 3

### APPROACH

This study focuses on delineating the orifice geometry that will provide optimal mixing at jet-to-main stream momentum-flux ratios and mass-flow ratios typical of RQL operating conditions.

The approach adapted for the present study was to measure the mixing of a scalar as the jets penetrated the core flow. The strategy adopted was to mix room temperature jets (i.e., cold jets) into a heated cross flow. Detailed measurements could then be acquired at selected axial planes.

To compare the mixing characteristics of different modules, it was decided that the temperature measurements would be normalized by defining a mixture fraction,  $f$ , at each point in the plane:

$$f = \frac{T_{mixed} - T_{jet}}{T_{main} - T_{jet}}$$

A value of  $f=1.0$  would correspond to the presence of pure main-stream fluid, while  $f=0$  would indicate the presence of pure jet fluid. Complete mixing occurs when  $f$  approaches the equilibrium value determined by the mass-flow ratio and temperatures of the jet and main-stream.

Five objectives were identified in Chapter 1 to accomplish the goals of (1) establishing criteria for the selection of an optimal mixer, and (2) identifying the optimal mixing configuration. To meet the goals and objectives of the present study, the following approach of four tasks was established:

Task I. Diagnostic Specification and Evaluation. Task I involved selecting an appropriate diagnostic method to be employed in the experiments. A thermocouple probe was chosen in accordance with the desire to use a simple and reliable measurement



technique that would perform the measurements. While the thermocouple probe simplified the diagnostic portion of the experiments, it provided an additional task of ensuring that the intrusive probe did not significantly perturb the flow field characteristics in the vicinity of the measurement point. Task I was satisfied by performing a series of experiments with different thermocouple arrangements to arrive at a design that provided a minimal degree of flow field disturbance. An additional series of experiments were performed to determine the necessary planar data point resolution to resolve the strong thermal gradients.

Task II. Test Matrix Specification. Task II entailed designing a test matrix that will facilitate a regression analysis to reveal the optimal mixing configuration. Several steps were involved in carrying out this task. First, the parameters of interest were identified. Then, the appropriate ranges of the parameters were selected such that the optimal mixing configuration fell within the limited range of the test matrix. Finally, the design and fabrication of the identified mixers followed directly from the parameter and range selection process.

Task III. Execution of Experiments. Task III encompassed conducting the experiments. The protocol for executing the experiments with the desired degree of resolution was established in Task I. The experiments were conducted as identified in Task II, with eight planes of data being acquired per mixing configuration. These data planes extended from one-tenth of an inch upstream of the leading edge of the orifices to one mixer radius downstream of the leading edge of the orifices. A series of repeatability experiments was conducted at one mixer radius downstream of the leading edge of the orifices to establish the degree of pure error involved in the experiments.

Task IV. Analysis. The repeatability experiments performed in Task III allowed the estimation of the degree of uncertainty involved in the selection of the optimal mixing configuration. The one mixer radius downstream plane ( $z/R=1.0$ ) was utilized in comparing the different mixers to one-another for the selection of the optimal

configuration. The temperature measurements were normalized to arrive at a mixture fraction value. A standard deviation of the mixture fraction (STD) was calculated at each plane in the flow field to quantify the degree of mixedness at any given plane. A regression analysis was performed on the results from the twenty-six experiments, i.e., thirteen full data sets plus the thirteen repeat experiments, at  $z/R=1.0$  to arrive at a model that quantifies the STD as a function of the number of orifices, the orifice aspect ratio, and the orifice angle. Several mixer configurations were closely examined to reveal the characteristics that gave rise to their relative performance.

## **CHAPTER 4**

### **EXPERIMENT**

#### **4.1 Facility**

The experimental facility that was used for this research is the same basic test stand and flow panel that is described in Hatch et al., 1992. For the sake of completeness, a brief overview of the facility is provided here.

##### **4.1.1 Flow Panel**

The air flow panel as shown in Figure 4.1, is divided into two circuits: a main flow circuit with a heater, and a jet flow circuit. The flow panel is supplied with filtered and dried air at 120 psig and approximately 74 °F. The primary pressure regulator provides the secondary pressure regulators with a steady supply of air at 100 psig. Each of the six secondary regulators is set at an outlet pressure of 75 psig to provide the flow metering valves with a steady and known supply pressure.

The main air circuit is divided into a course adjustment line (Main #1) and a fine adjustment line (Main #2). The two lines are used in concert to provide a precisely metered main air supply. Main circuits #1 and #2 are combined prior to entering the 20 KW electric heater. The air flows through a length of insulated 2 inch diameter steel pipe upon exiting the heater at the user prescribed temperature. This pipe is joined to a 2 inch diameter braided steel hose as shown in Figure 4.2, which allows the test assembly to enjoy three degrees of translational freedom. The braided hose is joined to a 2 feet long 4 inch diameter steel tube, to which the mixing module is attached.

##### **4.1.2 Test Stand**

The test stand was configured with optical diagnostic capabilities in mind, and as such, the diagnostics are fixed to the optical table while the test assembly is traversed. Figure 4.2 depicts the arrangement of the test assembly and the thermocouple probe. The

displacement of the three axes was monitored with a Mitutoya digital displacement indicator with a precision of 0.001 inch. The 1/8 inch type K thermocouple used for thermal flow field mapping was centered and aligned prior to each experiment.

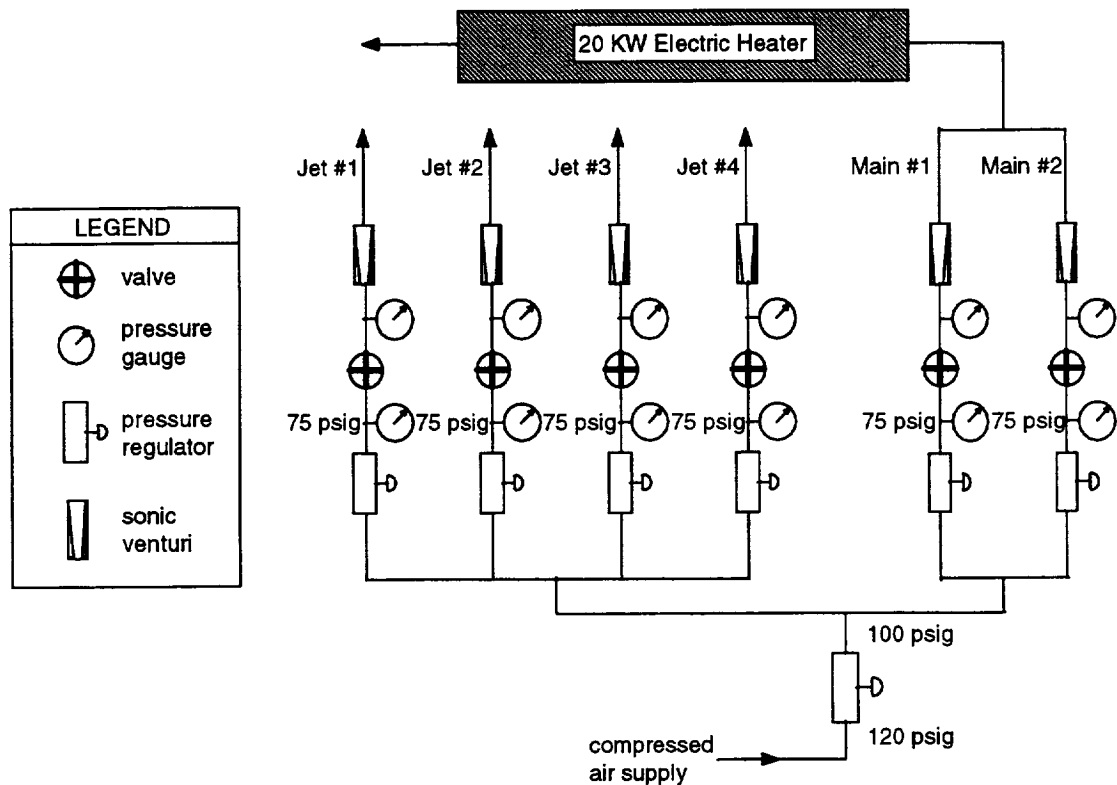


Figure 4.1 Flow Panel Schematic (adopted from Hatch et al., 1994)

A detailed view of the test assembly is shown in Figure 4.3. The main (core) air flow enters the bottom of the mixing module at a temperature of 212 °F.

The manifold was manufactured with four ports equally spaced around the manifold's circumference at both the top and bottom. Four individually metered air streams supply the lower four manifold ports with jet air at approximately 74 °F. After entering the bottom of the manifold, the jet air flows upward through a 1/2 inch thick

honeycomb ring. The honeycomb aids in removing any swirl from the jet air prior to its passage through the mixer's orifices.

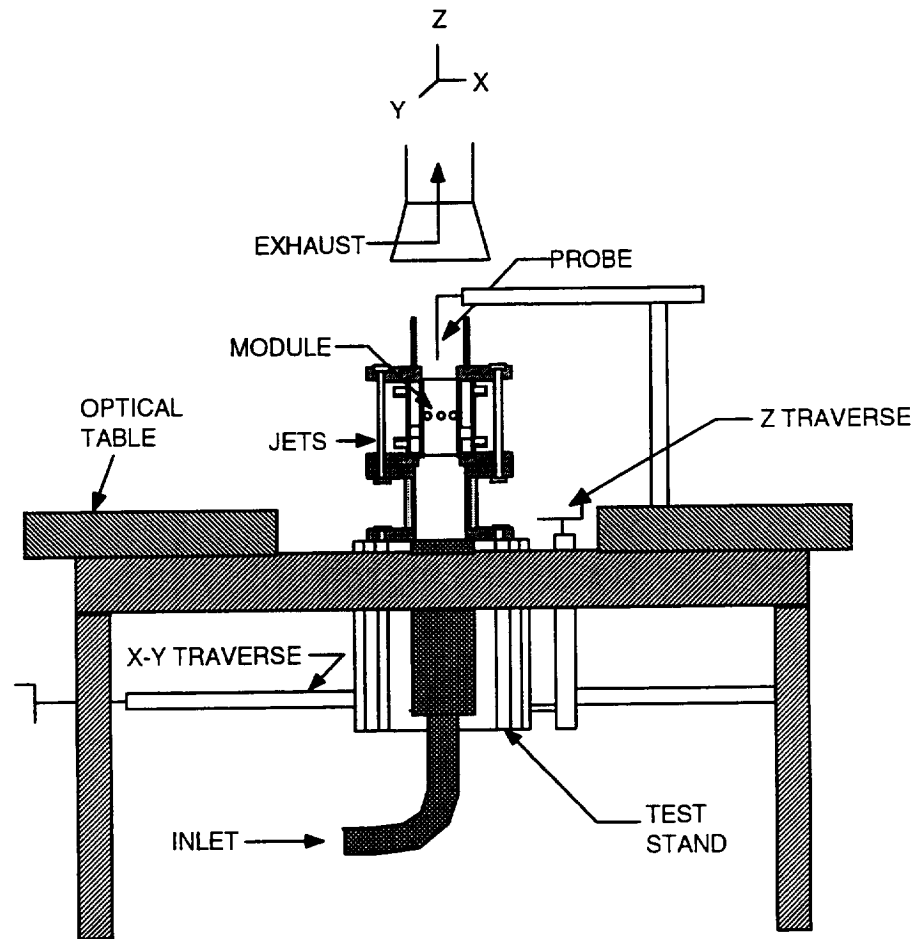


Figure 4.2 Test Stand Schematic (from Hatch et al., 1994)

One of the manifold's top ports is used to monitor the air pressure, a thermocouple is located in a second port to measure the jet temperature, and the remaining two ports are capped off.

A dimensioned mixer is shown in Figure 4.4 for reference.

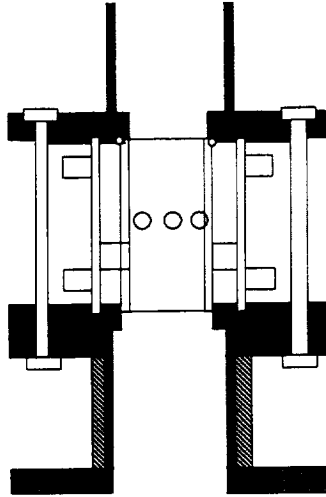


Figure 4.3 Test Assembly

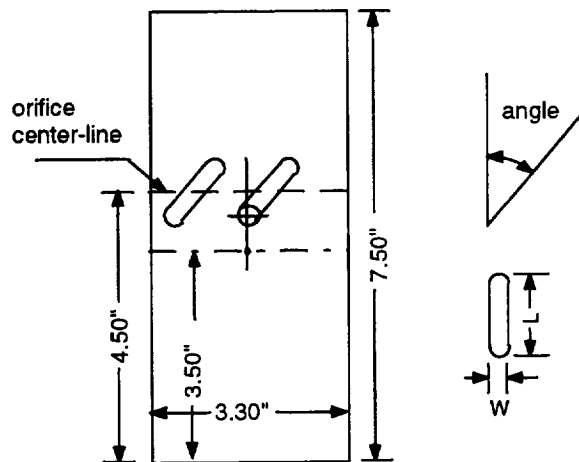


Figure 4.4 Mixing Module Dimensions

## 4.2 Diagnostics

Task I involved selecting an appropriate diagnostic method to be employed in the experiments. A thermocouple probe was chosen to perform the point temperature measurements in accordance with the desire to use a simple and reliable measurement technique. The logic behind this decision was that an easy to apply, fundamental technology would allow the bulk of the experimental effort to be focused on the data

collection and analysis processes, as opposed to spending a significant amount of time developing a more sophisticated diagnostic technique.

The relatively large time constant of the thermocouple had the effect of averaging the temperature fluctuations in the fully turbulent flow field.

#### **4.2.1 Thermocouple Probe Design**

Each probe design that was evaluated was a 12 inch long 1/8 inch diameter type-K thermocouple. The objective of the probe design analysis was to minimize the flow field perturbations caused by the probe in the subsonic jet and main air streams. The following criteria were established to evaluate alternative probe designs:

- The calculated jet fluid back-flow should be minimized and approach zero.
- 100% of the jet fluid mass should be accounted for at the orifice trailing edge plane ( $z/d = 1.0$ ).
- Deviation of the mean mixture fraction from the calculated equilibrium value at  $z/R=1.0$  should be minimized.

The initial probe design was a straight, axially-aligned type as shown in Figure 4.5. The theory behind this design was that the majority of the fluid flow was in the axial (z-axis) direction; hence any flow field disturbance would be minimized by aligning the probe with the bulk fluid motion.

For the straight axial-aligned probe, flow field perturbations were not significant except in the orifice region. In the vicinity of the orifices, the strong degree of cross-flow normal to the probe can cause perturbations that result in the appearance of a high degree of jet fluid back-flow; (i.e., the propagation of jet fluid in the upstream direction).

To minimize the perturbations in the orifice region, three other thermocouple arrangements were analyzed. The first was an axially aligned probe with a 90 degree bend near the thermocouple junction. In this arrangement, the 90 degree section of the probe pointed into the oncoming jet stream, thereby eliminating the strong cross-flow that the straight probe faced. Analysis of a data set collected with the 90 degree probe

revealed that this arrangement under-predicted the jet back-flow. Where the straight probe was unrealistically cold in the orifice region (biased to the jets), the 90 degree probe was unrealistically hot (biased to the main stream). In both cases, the cross-stream fluid tended to bias the measurement.

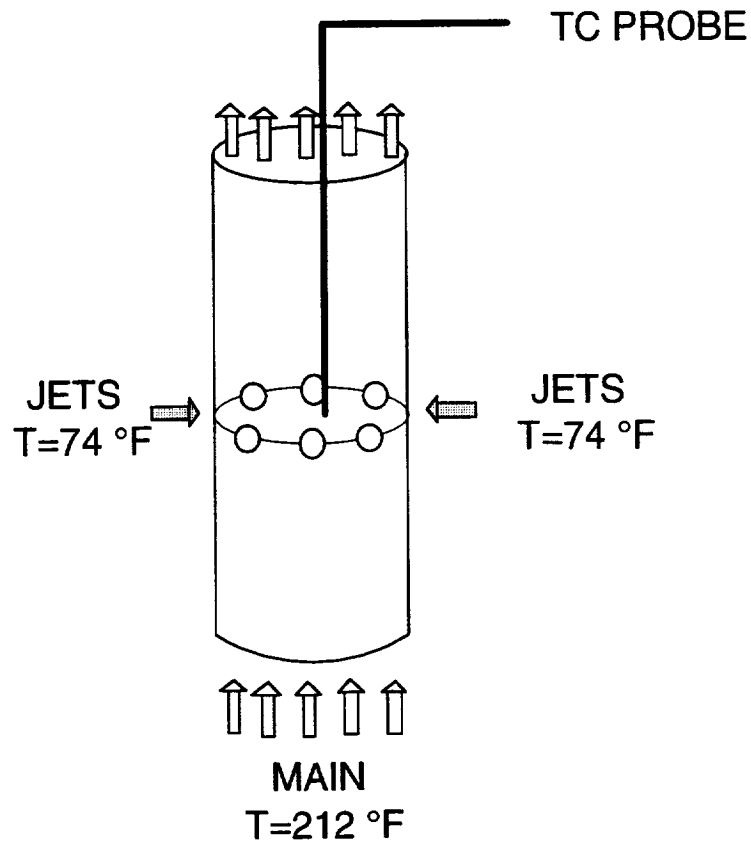


Figure 4.5 Straight Axial-Aligned Probe

On the basis of these results, an axially aligned probe with a 45 degree bend was selected and a third data set was collected for the same module (12 orifice round hole design at a jet-to-mainstream momentum-flux ratio of 36). Figure 4.6 depicts the results of the three data sets. This figure reveals that the 45 degree probe yields measurements that fall in-between the two extremes.



The percentage of the total jet mass accounted for at each axial plane of the orifice was also examined. The following relation was utilized to calculate the percentage of the total jet mass present at a given plane:

$$\% \text{ mass addition} = 100 * \frac{f_{eq}}{\bar{f}_i} * \frac{1 - \bar{f}_i}{1 - f_{eq}}$$

$\bar{f}_i$  is the average mixture fraction value at the  $i$ th plane and  $f_{eq}$  is the equilibrium mixture fraction value after all of the jet fluid has been added. This equation provided a means of tracking the jet fluid mass addition rate as a function of axial distance. (The derivation of this equation is provided in Appendix A.)

Figure 4.7 is used to illustrate the concept of the normalized axial direction ( $z$ ) with respect to the orifice axial height ( $h$ ).

The straight probe indicated that the mass addition process was complete near the middle of the orifice plane. The 45 degree probe indicated that the mass addition process was complete near the trailing edge of the orifice plane. The 90 degree probe indicated that the mass addition process continued beyond the trailing edge of the orifice plane.

An additional concern regarding the probe perturbation was the possibility that thermal conductance through the probe's sheath could bias the measurements. All three of the previously mentioned probes were shielded and grounded designs, meaning that the thermocouple junction was shielded by a metallic sheath, and physically joined (grounded) to the sheath at the tip of the probe. The possibility of thermal conductance biasing the measurements was removed by utilizing an exposed junction thermocouple and performing an additional experiment with a 45 degree exposed junction probe.

Figure 4.8 illustrates two of the data sets that were taken for the 8 circular orifice modules at a jet-to-mainstream momentum-flux ratio ( $J$ ) of 73. The two different 45 degree data sets are nearly identical, thereby eliminating the concern of thermal conductance biasing. However, the faster response time of the exposed junction thermocouple, and the ability to align the relatively small exposed junction with greater

precision, makes the 45 degree exposed junction thermocouple the best arrangement tested.

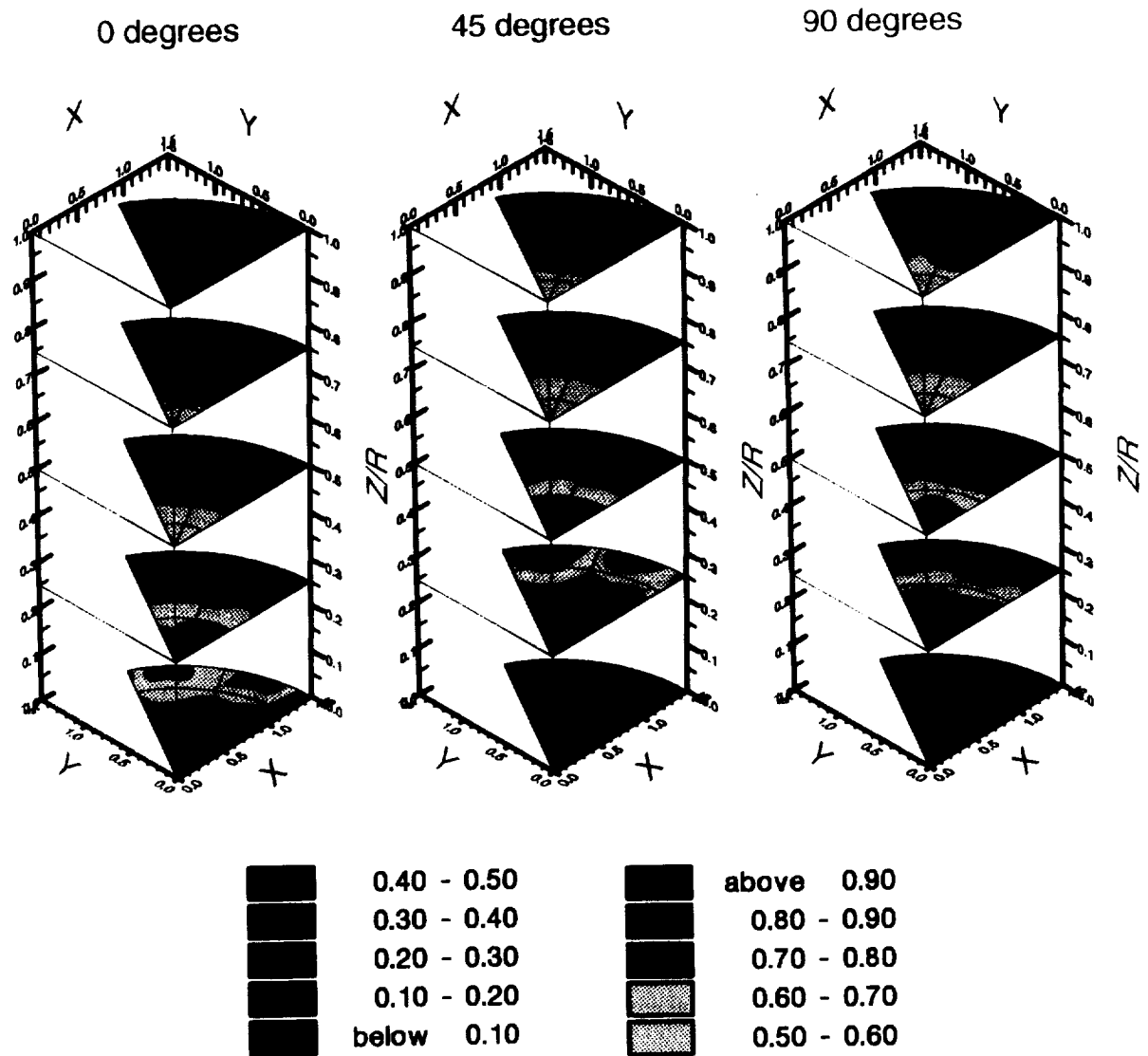


Figure 4.6      Effect of variations in thermocouple probe orientation on mixture fraction for 12 circular orifice J=36 module.

#### 4.2.2 Data Resolution between Measurement Planes

Each of the orifice optimization experiments involved the measurement of the eight planes of data that are illustrated in Figure 4.9. Six of the eight data planes were concentrated in the orifice region where the strongest thermal gradients were located. The decision was made to make measurements at a total of eight planes based on a compromise between the desire to map out the thermal profiles with fine detail, and the need to limit the amount of time associated with each experiment to a reasonable length.

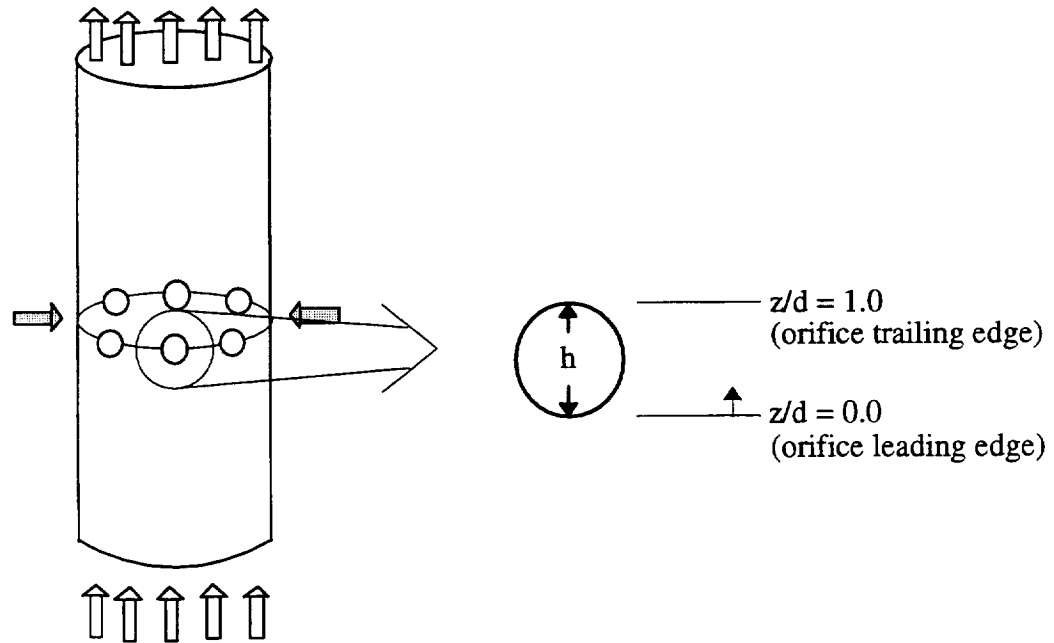


Figure 4.7 Orifice Plane Terminology

Shielded 45 Degrees

Exposed 45 Degrees

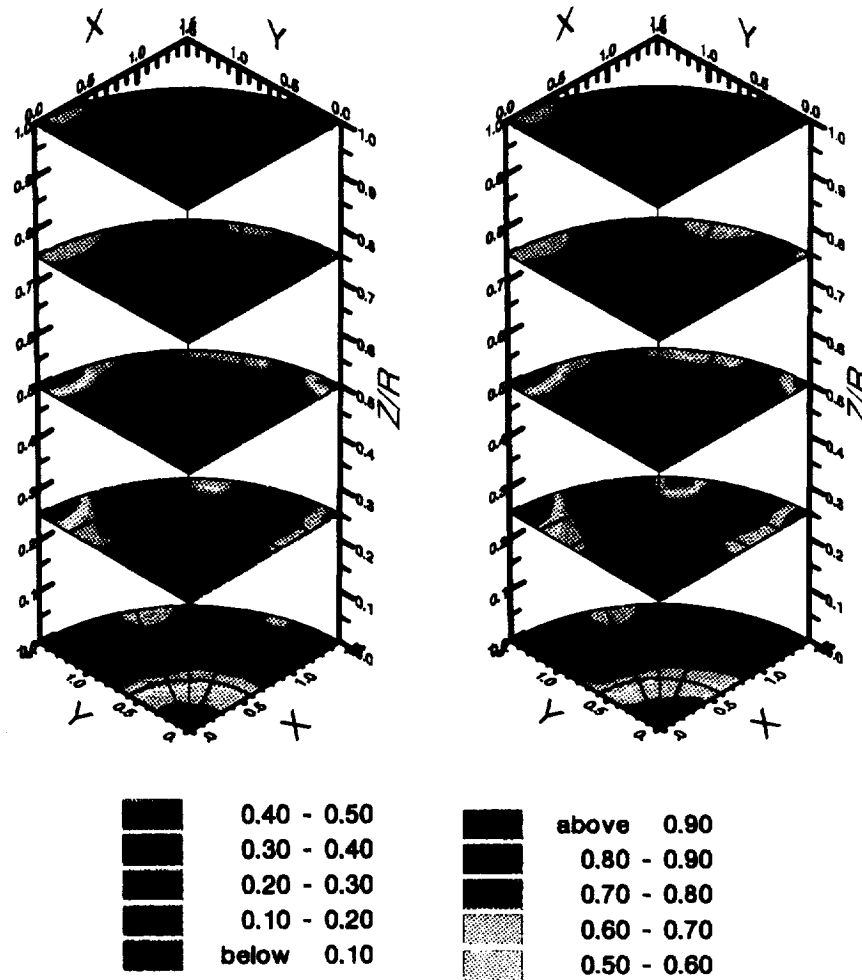


Figure 4.8 Effect of variations in thermocouple probe orientation on mixture fraction for 8 circular orifice J=73 module.

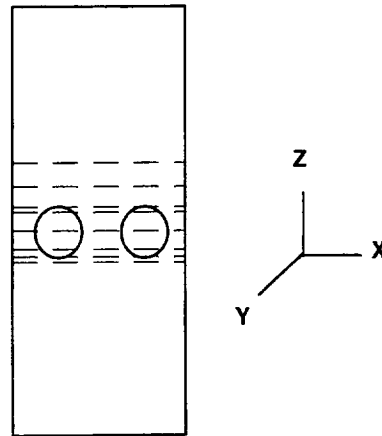


Figure 4.9 Measurement Planes

These eight planes were located based on the following relationships expressed in units of inches:

Plane 1:	$z = -0.100$
Plane 2:	$z = 0.000$
Plane 3:	$z = 0.100$
Plane 4:	$z = h/2$
Plane 5:	$z = h - 0.100$
Plane 6:	$z = h$
Plane 7:	$z = h + (R - h)/2$
Plane 8:	$z = R$

where  $h$  = the orifice axial height and the mixer radius,  $R = 1.500$  inches.

A linear interpolation scheme was employed to arrive at 100 equally spaced data planes between  $z = 0.0$  and  $z = R$ .

#### 4.2.3 Data Resolution between Measurement Points

Temperature measurements revealed variations in the strength of the jet flow through each orifice. While these jet-to-jet variations were acceptable, they precluded using the temperature profile of a single orifice sector as representative of the entire mixer cross-section. Figure 4.10 illustrates a single and a dual orifice sector.

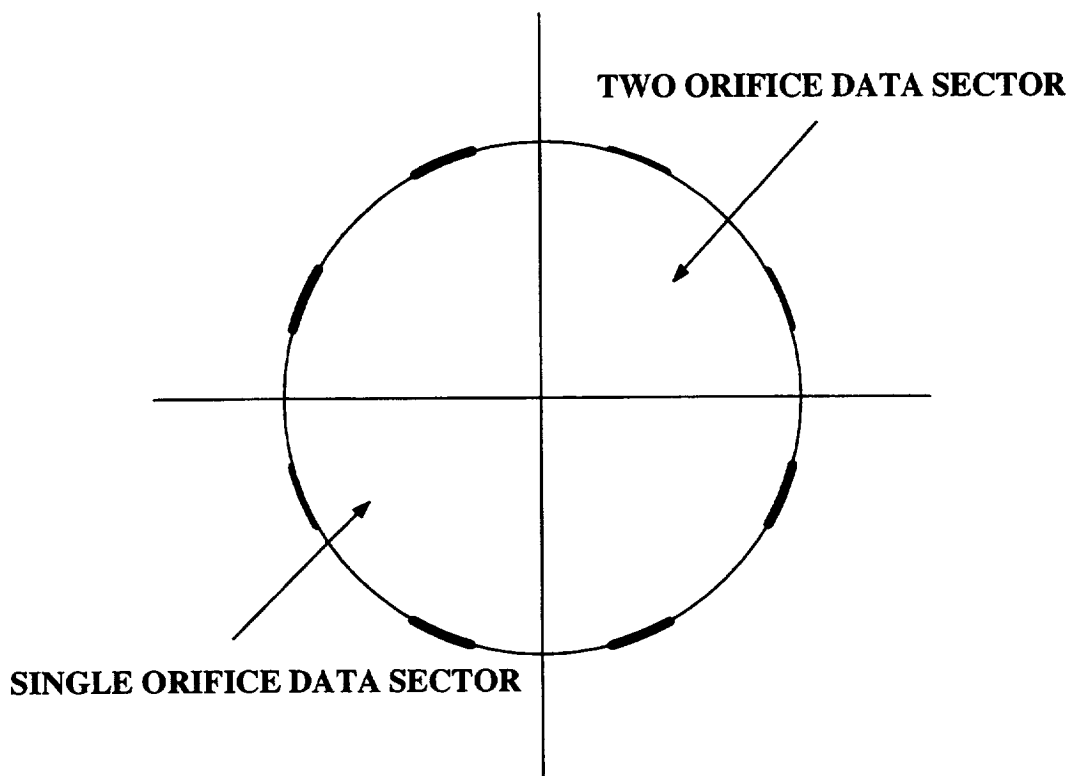


Figure 4.10 Eight orifice module data sectors for single and dual orifice mapping

Two sets of data were collected to estimate the error involved in using a dual orifice sector as representative of the entire mixer cross-section. The mixer type involved in this analysis was an eight circular orifice design. A two orifice ( $90^\circ$ ) sector of data at  $z/R=1.0$  was compared to a four orifice ( $180^\circ$ ) sector of data. The analysis revealed that the same mixing performance conclusions would be reached with either data set. On the basis of this observation, each data set was tailored to a two orifice sector for all subsequent experiments.

One further resolution question involved the spatial measurement grid density within the two orifice sector. The same dilemma was involved in this choice as was involved in determining the number of data planes to measure, i.e., the desire to map out the thermal profiles with fine detail versus the need to limit the amount of time associated

with each experiment. Figures 4.11, 4.12, and 4.13 represent sequential enhancements in grid density resolution for a two orifice  $90^\circ$  sector. Each point represents a spatial location on a given axial plane where a temperature measurement was made.

The initial orifice sector grid is shown in Figure 4.11. It is composed of 50 points dispersed across equal area sectors. Analysis of the thermal contours of sequential axial data planes for a given mixer with this grid density revealed the need for a greater degree of resolution. One observed problem was the virtual disappearance of the cold jet fluid thermal contours. The problem was due to the relatively large angle between adjacent radial data point lines. This gap allowed the jet fluid to remain hidden from the measurements.

The data grid shown in Figure 4.12 involved roughly doubling the number of data points to 108 by increasing the number of radial data lines and adding one additional equal area sector. This scheme was improved upon by the grid shown in Figure 4.13. This grid utilizes 122 data points in a different manner than the two previous grids. The central portion of the grid is composed of a Cartesian type of scheme employing equal x,y increments. Additionally, data points are arranged in an equal increment fashion along the initial and final sector radial lines, as well as around the circumference of the sector.

A grid of the type shown in Figure 4.12 was used for the circular orifice optimization experiments, while the global orifice optimization experiments used a grid of the type shown in Figure 4.13.

### **4.3 Test Matrix Specification**

Preliminary experiments were conducted to establish the effect of the orifice geometry on jet penetration. In particular, these experiments examined the relationship between jet penetration, orifice design, and the number of orifices for differing jet-to-main flow momentum-flux ratios ( $J$ ). Jet penetration characteristics as a function of orifice design were investigated at momentum-flux ratios of 25 and 52. An additional

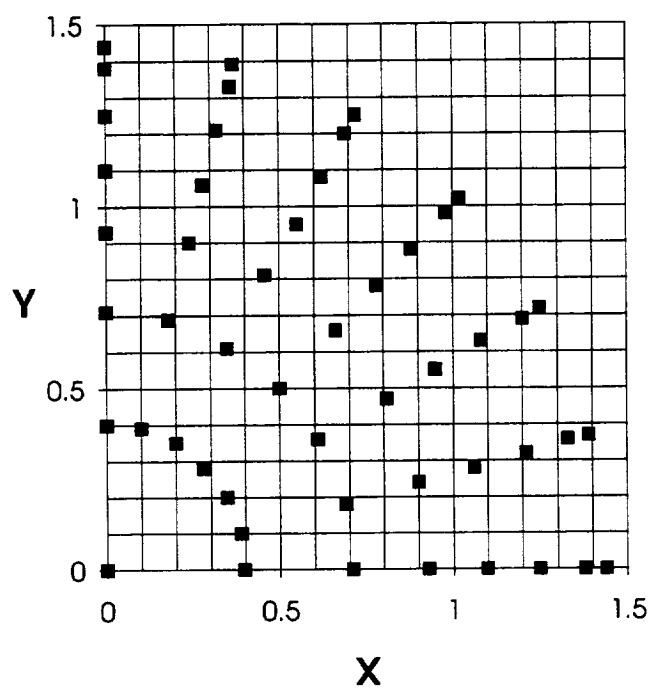


Figure 4.11 Planar Data Point Grid of Sparse Density

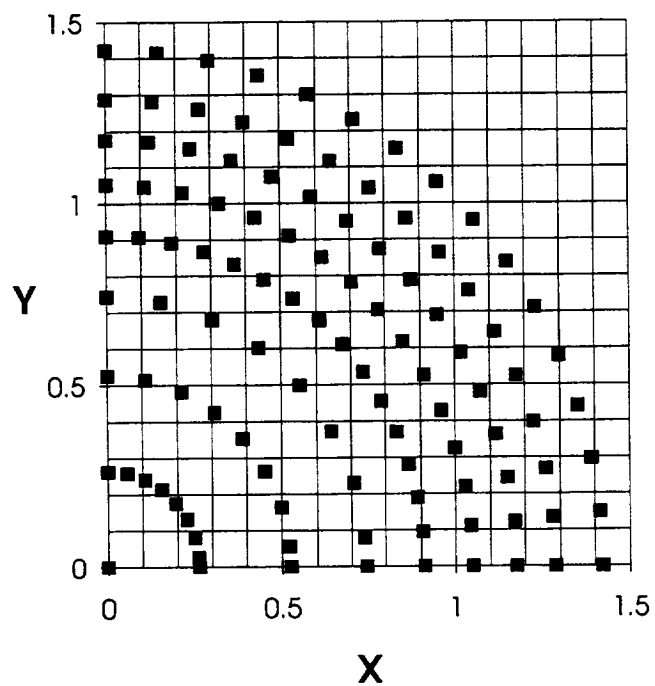


Figure 4.12 Planar Data Point Grid of Intermediate Density



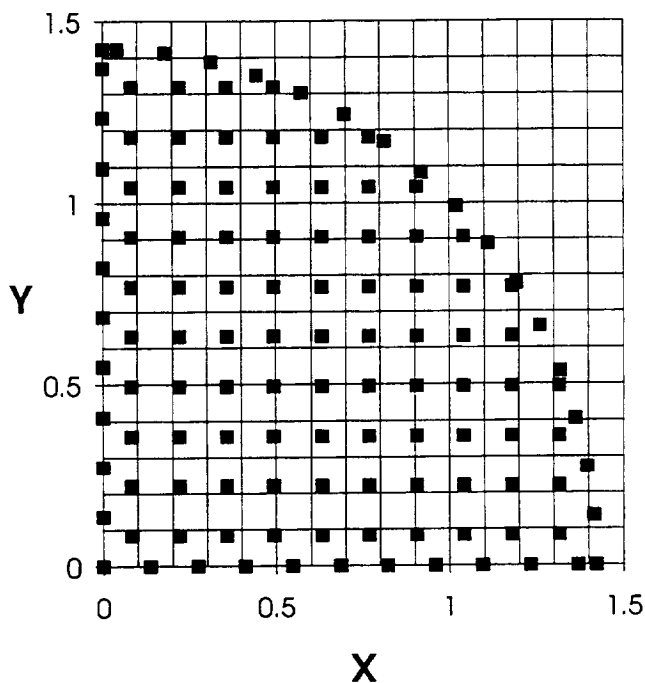


Figure 4.13 Final Planar Data Point Grid Density

series of experiments was conducted to optimize the mixing characteristics of circular orifices at momentum-flux ratios of 36 and 73. On the basis of these results, a Box-Behnken test matrix was established for the global optimization study.

#### 4.3.1 Jet Penetration as a Function of Orifice Design

Experiments were conducted to illuminate the relationship between jet penetration and orifice design. Criteria were defined to aid in selecting the best mixer based on the center line mixture fraction ( $f$ ) plots. As such, the mixture fraction should be approximately equal to one at  $z/R=0.0$ , whereas  $f \ll 1.0$  at the orifice leading edge plane would indicate jet over penetration. An additional indicator of over penetration is when the mixture fraction is much less than the equilibrium mixture fraction at  $z/R=1.0$ .

#### 4.3.2 Circular Orifice Optimization

A series of experiments was conducted to determine the influence of the number of circular orifices on mixing of jets in a can geometry. The experiments were conducted at momentum-flux ratios of 36 and 73, while maintaining a jet to mainstream mass flow

ratio of 2.2. The number of orifices was varied from 6 to 12 at  $J=36$ , and from 6 to 18 at  $J=73$ . The findings of these experiments are presented in Chapter 5.

### 4.3.3 Global Orifice Optimization

On the basis of the results of the proceeding two sets of experiments, a Box-Behnken test matrix was designed to encompass the optimal mixing geometry at a momentum-flux ratio of 40. A fixed jet-to-main stream mass flow ratio of 2.5 was selected for these experiments. The mixture fraction standard deviation (STD) was calculated at each plane in the flow field to quantify the degree of mixedness at any given plane. A regression analysis was performed on the results at the  $z/R=1.0$  plane to arrive at a model that quantifies the STD as a function of the number of orifices, the orifice aspect ratio, and the orifice angle. A description of the analysis follows in Section 4.5.

The particular attraction of a Box-Behnken test matrix is that it allows the fitting of non-linear models to the data while minimizing the number of required experiments. Thirteen different geometric configurations were designed, manufactured and tested with each experiment being repeated once to provide an estimate of pure experimental error. The repeat tests brought the total number of experiments to twenty-six. A cubic model was fitted to the twenty-six data sets.

The 13 experiments to be conducted at  $J=40$  are tabulated in Tables 4.1 and shown pictorially in Figure 4.14.

## 4.4 Execution of Experiments

The Box-Behnken test matrix experiments (optimization experiments) were conducted based on the protocol outlined in Section 4.2. An axial aligned 12 inch long 1/8 inch diameter type K exposed junction thermocouple was used to make the temperature measurements. The probe was bent at a  $45^\circ$  angle at a distance of two inches from the junction. A two orifice sector was probed for each mixer. The thermocouple probe junction was aligned with the center of the mixer's cross-section, with the  $45^\circ$  angle of the probe pointing toward the center of the sector to be probed.

Table 4.1 Box Behnken Test Matrix

CASE	NUMBER OF ORIFICES	ASPECT RATIO	SLOT ANGLE
1	16	5	30
2	16	3	0
3	16	3	60
4	16	1	30
5	12	5	0
6	12	5	60
7	12	3	30
8	12	1	0
9	12	1	60
10	8	5	30
11	8	3	0
12	8	3	60
13	8	1	30

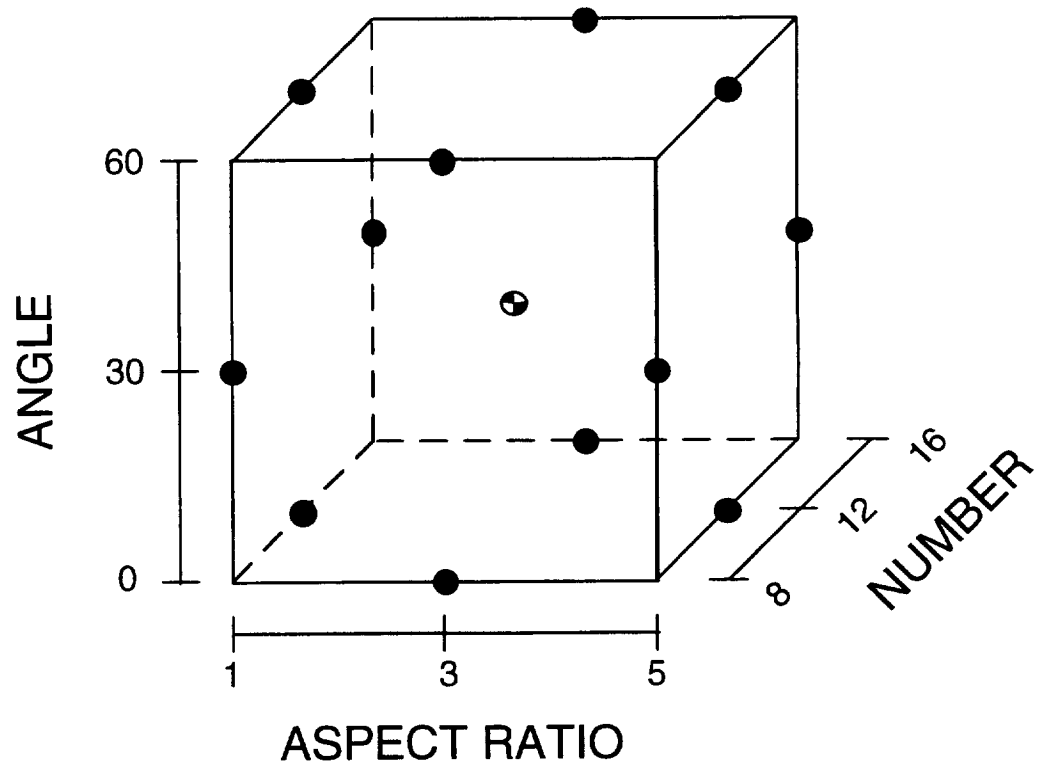


Figure 4.14 Graphical illustration of Box-Behnken test matrix.

Eight planes of data were measured for each module as described in Section 4.2.2. Following the completion of the 13 experiments, an additional sector of data at  $z/R=1.0$  was repeated to allow the estimation of the experimental uncertainty.

#### 4.5 Analysis

The mixture fraction value is a measure of the degree of local mixedness or unmixedness at a given point. Temperature measurements were made as a means of tracking the local mixture fraction. This was possible due to the non-reacting nature of the experiments. In this system, temperature is a conserved scalar (i.e. no sources or sinks), and as such, can be used to track any other conserved scalar with equal diffusivities such as local species concentrations in a non-reacting system (Smoot and Smith, 1985).

The Lewis number (Le), defined as the ratio of the Schmidt number and the Prandtl number, is a non-dimensional parameter that relates the thermal and mass diffusivities.

$$Le = \frac{\lambda}{\rho c_p D_{ij}} = \frac{\alpha}{D_{ij}}$$

The question arose whether the mixture fraction can track both the thermal and the species mixing in the current experiment. The Lewis, Schmidt, and Prandtl numbers are commonly equated to unity when modeling turbulent reacting flows (Kuo, 1986 and Glassman, 1987). This assumption is being followed in this study as well.

The mixture fraction takes the following form when based on temperatures (see the derivation in Appendix A for more detail):

$$f = \frac{T_{mixed} - T_{jet}}{T_{main} - T_{jet}}$$

A value of  $f=1.0$  corresponds to the presence of pure main-stream flow, while  $f=0$  indicates the presence of pure jet flow. Complete mixing occurs when  $f$  approaches the

equilibrium value determined by the mass flow ratio and temperatures of the jet and main-stream.

The following relation was utilized to calculate the percentage of jet mass added at a given plane:

$$\% \text{ jet mass added} = 100 * \frac{f_{eq}}{\bar{f}_i} * \frac{1 - \bar{f}_i}{1 - f_{eq}}$$

$\bar{f}_i$  is the average mixture fraction value at the  $i$ th plane and  $f_{eq}$  is the equilibrium mixture fraction value after all of the jet fluid has been added. This equation provided a means of tracking the jet fluid mass addition rate as a function of axial distance. The derivation of the percentage of jet mass added equation is included in Appendix A.

To quantify the mixing effectiveness of each mixer configuration, an area-weighted standard deviation parameter ("STD") was defined at each measurement and interpolated data plane.

$$STD = \sqrt{\frac{1}{A} \sum a_i (f_i - \bar{f})^2}$$

$f_i$  is the average planar mixture fraction,  $a_i$  is the nodal area at which  $f_i$  is calculated, and  $A = \sum a_i$ . It should be noted that at planes downstream of the trailing edge of the orifice,  $\bar{f}$  equals the equilibrium mixture fraction. Complete mixing is achieved when the STD across a given plane reaches zero.

A statistical analysis package from the Statistics Department of Brigham Young University called Rummage II was used to perform the regression analysis on the STD results to arrive at an interpolating equation for the STD as a function of the number of orifices, the orifice aspect ratio, and the orifice angle. The regression equation is a second order polynomial. Significance testing is used to remove insignificant terms in the equation. The interpolating equation does not have any physical significance. Its form is chosen to describe areas of curvature in the response variable of interest such that reasonable interpolation can be done between observations.

## **CHAPTER 5**

### **RESULTS AND DISCUSSION**

Evaluation of jet penetration was done to lay the foundation for optimization experiments that follow. The jet penetration study focused on the centerline mixture fraction values and the degree of penetration at the leading edge of the orifices.

The optimization experiments were divided into two test matrices: one addressing circular orifice optimization and the other addressing “global” optimization. The circular orifice optimization experiments sought to illuminate the role of jet penetration depth on mixing. The term “global” refers to the design space of the orifice geometry parameters. The global optimization experiments utilized the insight gained from the experiments that preceded the present study, and broadened the objective from determining the value of a single orifice design parameter for best mixing, to determining the best combination of all three orifice design parameters (i.e., number of orifices, orifice long-to-short side aspect ratio, and orifice angle).

#### **5.1 Jet Penetration as a Function of Orifice Design**

Figures 5.1, 5.2, and 5.3 depict the mixture fraction along the center line of the mixing module as a function of non-dimensional axial distance. Included on each plot is a vertical line at  $z/R = 0.0$  indicating the leading edge plane of the orifices, and a horizontal line at the equilibrium mixture fraction value ( $f = 0.3125$ ). Each of the figures is composed of three plots, with each plot depicting the results of the six and ten orifice modules at the indicated momentum-flux ratio for a particular orifice geometry. Figure 5.1 depicts the results for the round hole modules at all three momentum-flux ratios ( $J = 25, 52$ , and  $80$ ). With the top plot displaying the  $J = 25$  results, the center plot

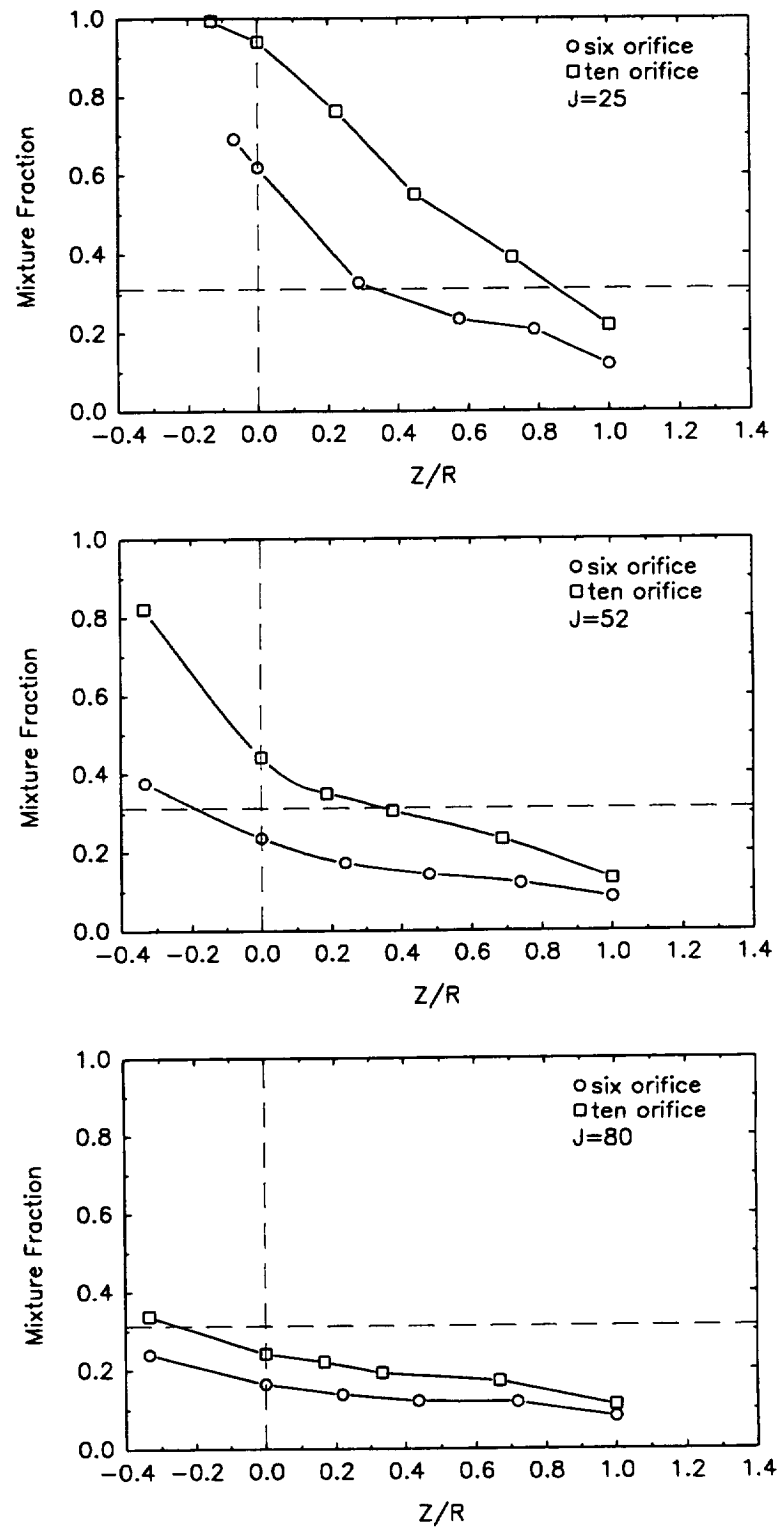


Figure 5.1 Center Line Mixture Fraction Measurements for Round Hole Modules

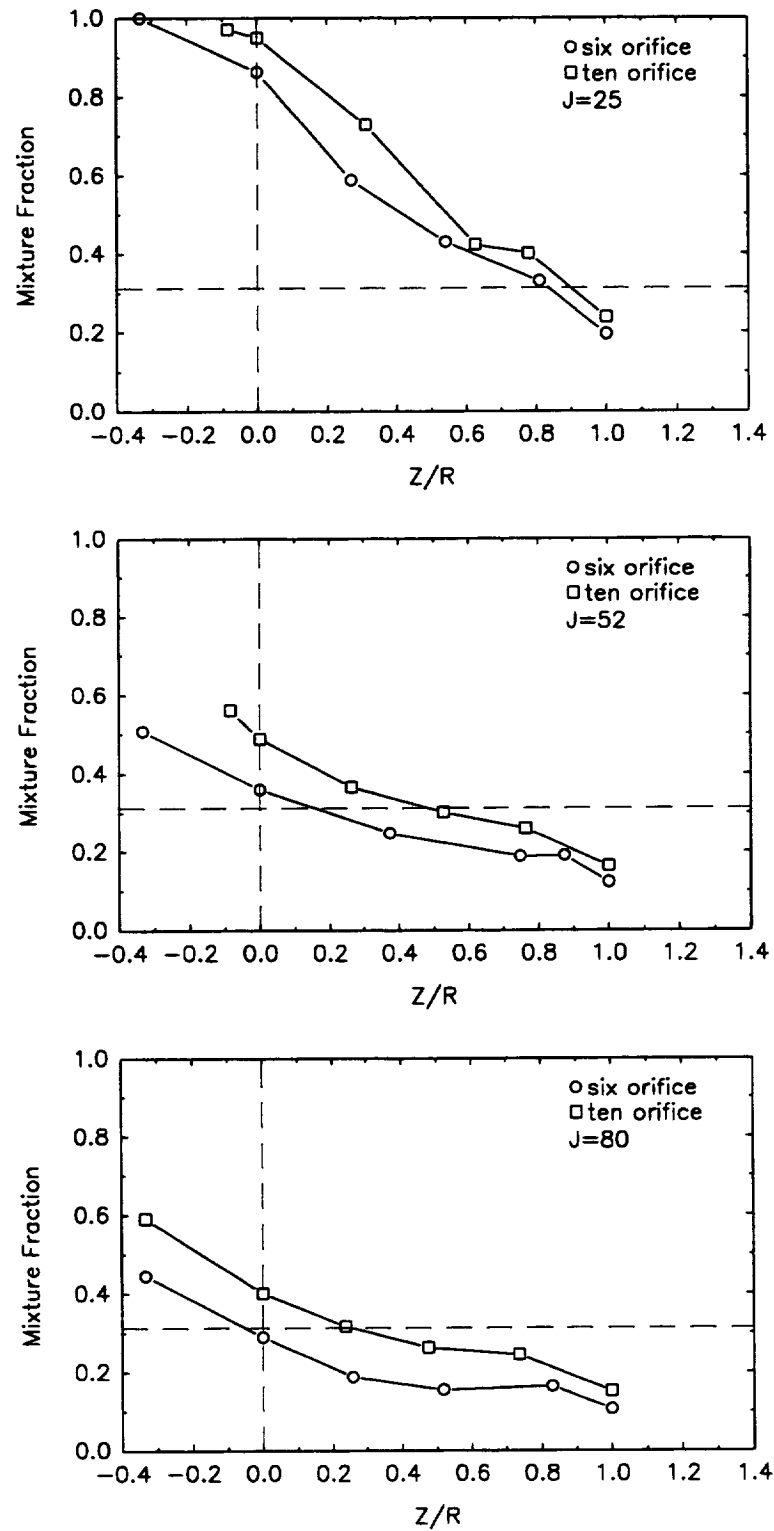


Figure 5.2 Center Line Mixture Fraction Measurements for 4:1 AR @ 45 degrees Modules



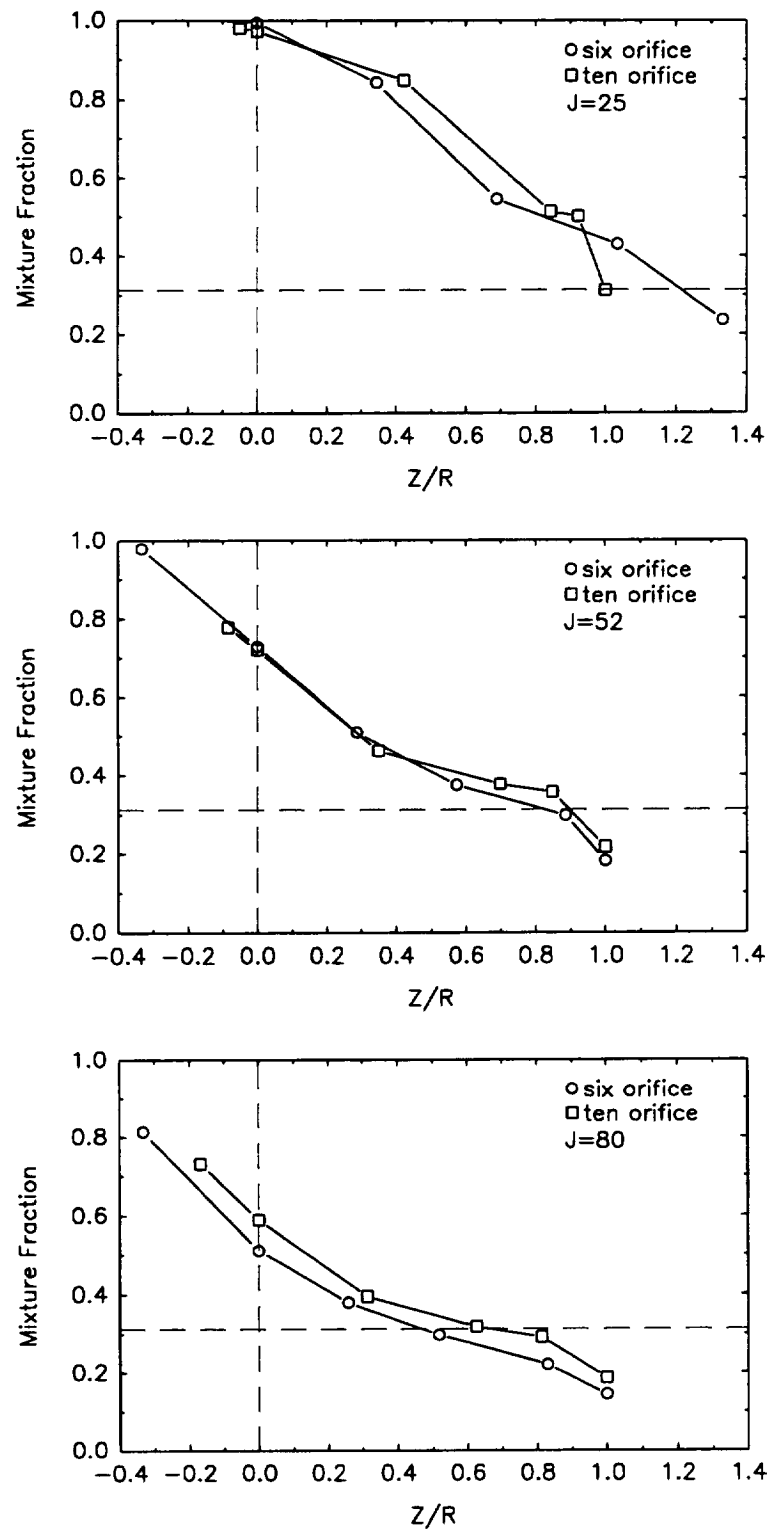


Figure 5.3 Center Line Mixture Fraction Measurements for 8:1 AR @ 45 degrees Modules

displaying the  $J=52$  results, and the bottom plot displaying the  $J=80$  results, the effect of momentum-flux ratio on jet penetration can be readily appreciated. The  $J=25$  ten orifice module can be identified as a near optimum mixer based on the criteria stated above. Likewise, the six and ten orifice modules at  $J=52$  and  $J=80$  are severely over penetrating.

One final comment regarding the round hole modules can be made concerning the percent difference in mixture fraction values between the six and ten orifice modules. In each of the three momentum-flux ratios, the percent difference in mixture fraction values between the six and ten orifice modules is approximately 50%. This indicates that jet penetration for the round hole orifice design is very responsive to variations in the number of orifices.

Figure 5.2 depicts the center line mixture fraction results for the mixing modules with 4:1 aspect ratio (AR) slots at 45 degree inclinations. Given this aspect ratio and angle, as with the round hole modules, it appears that the ten orifice  $J=25$  module is closest to the optimized configuration. This orifice design exhibits approximately 20% difference between the six and ten orifice modules.

Figure 5.3 displays the results for the 8:1 AR 45 degree slots. In agreement with the modules in Figures 5.2 and 5.3, the results in Figure 5.3 indicate that the ten orifice module is near the optimal configuration at  $J=25$ , while the same number of orifices is severely over penetrating at  $J=52$  and  $J=80$ .

An immediate observation regarding Figure 5.3 is the amazing degree of similarity in measurements for the six and ten orifice modules at all three momentum-flux ratios. The  $J=25$  and  $J=52$  modules have a percent difference of approximately zero, while the  $J=80$  modules have a slightly greater difference in results, but still much less difference than the other orifice designs.

On the basis of the results presented in Figures 5.1, 5.2 and 5.3, the ten orifice modules perform better than the six orifice modules for all three orifice designs.

However, the ten orifice modules over penetrate for all three orifice designs at  $J=52$  and  $J=80$ .

Perhaps the most striking observation to be made from these data is that the degree of jet penetration sensitivity to variations in the number of orifices decreases as the slot aspect ratio increases. (The round hole orifices can be considered as the special case of an aspect ratio of 1.) This suggests that there may be a greater potential for optimization for the round hole modules.

## 5.2 Circular Orifice Optimization

A series of experiments was conducted to determine the influence of the number of circular orifices on mixing of jets in a can geometry in general, and the role of jet penetration in particular. The parametric experiments were investigated at momentum-flux ratios of 36 and 73, while maintaining a jet to mainstream mass flow ratio of 2.2. These values were selected as representative of practical applications.

Table 5.1 summarizes the mixer types that were considered. Also tabulated is the axial location of the trailing edge of the orifice ( $d/R$ ), and the percentage of circumferential orifice blockage. The former is expressed as the ratio of the diameter of the orifice ( $d$ ) to the radius of the mixing module ( $R=1.5$  inches), and the latter is defined as the ratio of the total circumferential projection of the orifices to the circumference of the mixing module.

The operating conditions are presented in Table 5.2. Reference velocity, defined as the velocity at the inlet to the mixing section and calculated based on the mainstream temperature and pressure, was 34.5 fps. As a note, all ratios (momentum-flux, mass, and density) are expressed as jet flow divided by main flow.

Of the three orifice parameters of interest (number of orifices, orifice long-to-short side aspect ratio, and orifice angle), only the number of orifices was varied with each orifice design being circular. Inasmuch as the trends are similar in both cases, the results for the experiments conducted at a momentum-flux ratio of 73 are discussed first

Table 5.1 Normalized Circular Orifice Axial Height and Percent Blockage

Momentum-Flux Ratio	Number of Orifices	d/R	Blockage (%)
J=36	6	0.58	56
J=36	8	0.50	64
J=36	10	0.45	72
J=36	12	0.41	78
J=73	6	0.48	46
J=73	8	0.42	53
J=73	10	0.37	60
J=73	12	0.34	65
J=73	15	0.30	73
J=73	18	0.28	80

Table 5.2 Circular Orifice Operating Conditions

T <sub>main</sub> (°F)	T <sub>jet</sub> (°F)	P (psia)	V <sub>main</sub> (ft/s)	M <sub>main</sub> (lbm/s)	Mass-flow Ratio	Density Ratio
212	74	14.7	34.5	0.10	2.2	1.26

followed by a summary of the results for the experiments conducted at a momentum-flux ratio of 36.

### 5.2.1 Mixing Downstream of the Orifice

It is necessary to examine the downstream mixing to better understand the mixing processes occurring in each module. In particular, the mean jet trajectory provides much insight into the overall mixing process. Figures 5.4 and 5.5 depict radial-axial slices, which have been selected near the center of the orifices, of mixture fraction values for J=73 and J=36 respectively. The mainstream is flowing from left to right, and the jet is discharging downward from the top of the figure toward the centerline of the module at the bottom of the figure. These figures were created by linearly interpolating between a maximum of eight measured data planes. They are, therefore, useful for trend analysis, but should not be considered absolutely quantitative at all points.

The intent of Figures 5.4 and 5.5 is to obtain an intuitive view of the jet trajectory. As such, they can be used to make qualitative comparisons between modules, but should

not be used to make quantitative comparisons. Additionally, note that these are specific radial-axial planes near the orifice center-line, and not an average over several planes.

In Figures 5.4 and 5.5, radial distance is measured from the module centerline ( $r/R=0$ ) to the module wall ( $r/R=1.0$ ). The axial distance is measured from the leading edge of the orifice ( $z/R=0$ ) to one duct radius downstream ( $z/R=1.0$ ). The mean jet trajectory can be traced by following the lowest values of mixture fraction downstream from their point of origin at the module wall. From these figures, it can be seen qualitatively that the mean jet trajectory is strongly correlated with the number of orifices.

Figure 5.6 illustrates different characteristics of the jet trajectory that can be estimated semi-quantitatively from Figure 5.4 and 5.5. In total, three characteristics have been examined: linear penetration depth, the mean jet penetration depth at  $z/R=1$ , and the likelihood that the mean jet trajectory will penetrate to the centerline of the module. Linear penetration depth characterizes the normalized distance from the module wall that the jet travels before deflection is apparent in the axial direction. The jet penetration depth was estimated from experimental data for the plane at one duct radius downstream of the leading edge of the orifice. It is a distance normalized by the module radius which tracks how far from the module wall the lowest mixture fraction value is found. The likelihood that the mean jet trajectory will intersect with the module centerline can be estimated based on observations of the mean jet penetration depth versus axial distance downstream of the orifice.

Table 5.3 summarizes the three characteristics discussed above for the  $J=73$  cases shown in Figure 5.4. It should be noted that of the six cases considered at  $J=73$ , only three had mean jet trajectories that likely intersected with the module centerline. It is also noteworthy that the 15 hole module which demonstrates the most uniform mixing at the trailing edge of the orifice had a jet penetration distance of only 44 percent of the module radius measured from the module wall. The  $J=36$  jet penetration results are similar to those discussed above, albeit the change from penetration that intersects the centerline to

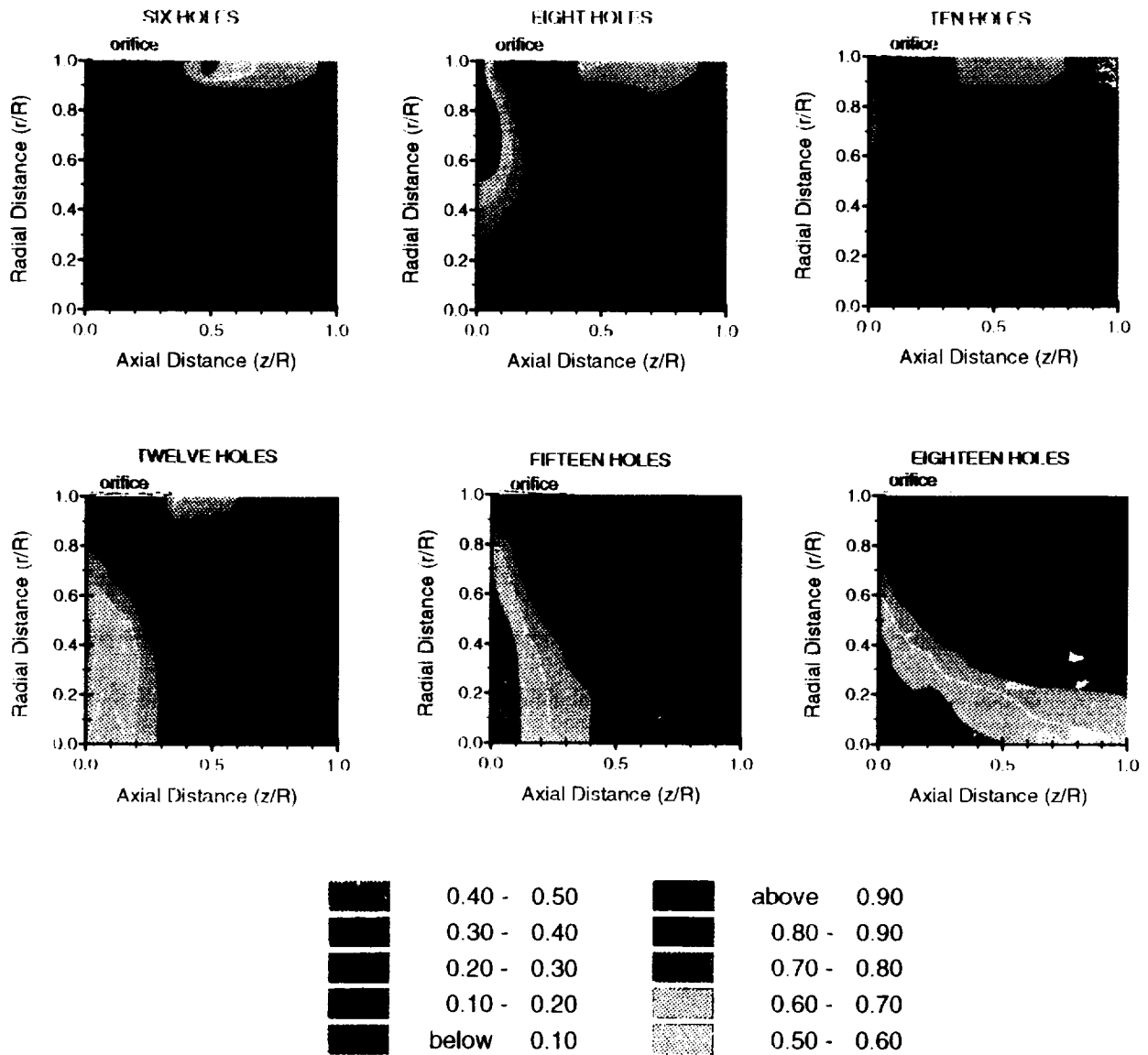


Figure 5.4 Local mixture fraction contours for the  $J=73$  momentum-flux ratio modules as the number of orifices is varied. Radial distance varies from the module's centerline ( $R=0$  inches) to the wall ( $R=1.5$  inches). Axial distance varies from the orifice leading edge ( $z=0$  inches) to one duct radius downstream ( $z=1.5$  inches).

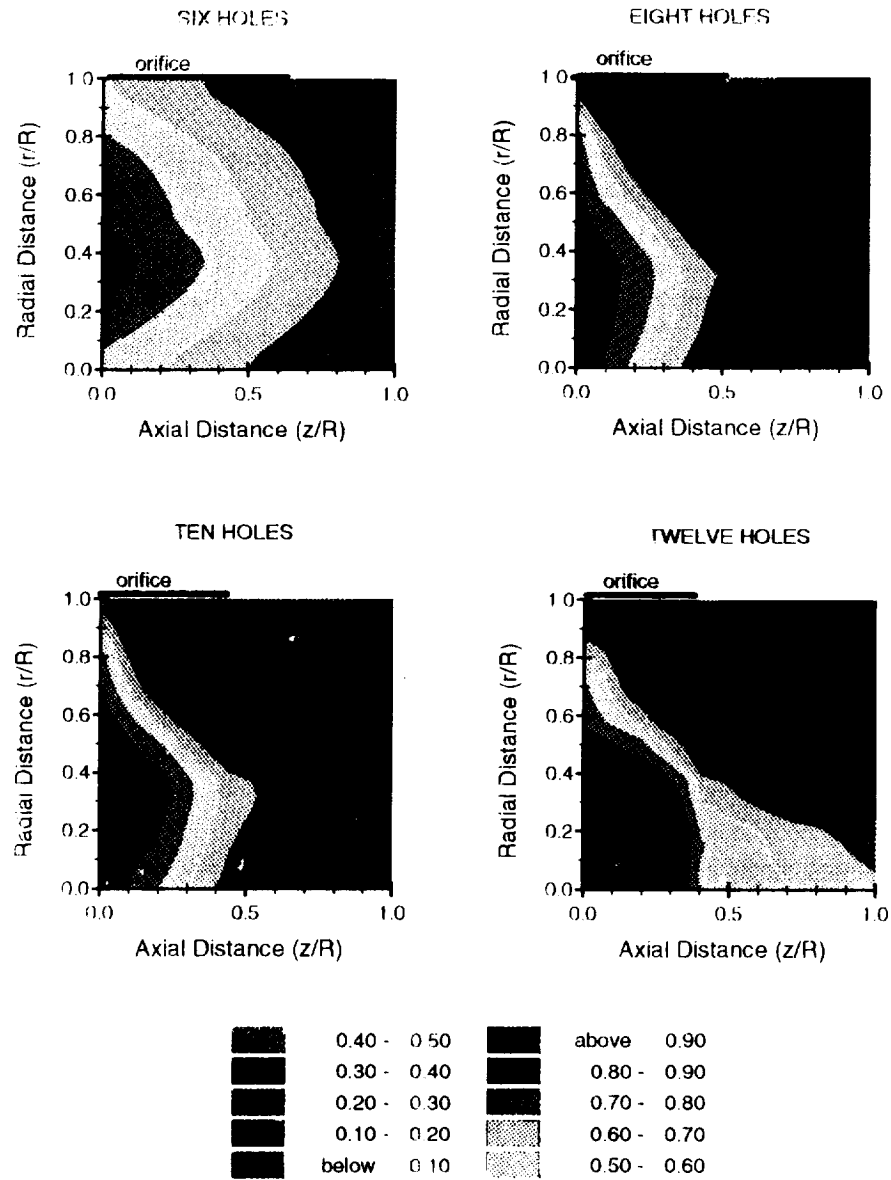


Figure 5.5 Local mixture fraction contours for the J=36 momentum-flux ratio modules as the number of orifices is varied. Radial distance varies from the module's centerline ( $R=0$  inches) to the wall ( $R=1.5$  inches). Axial distance varies from the orifice leading edge ( $z=0$  inches) to one duct radius downstream ( $z=1.5$  inches).

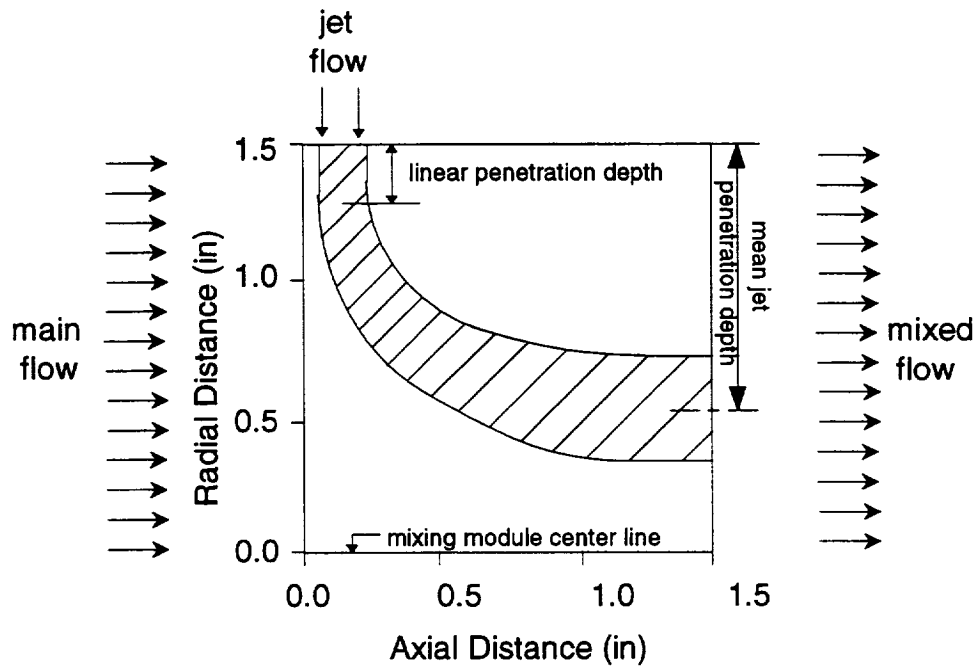


Figure 5.6 Example of Jet Trajectory Features Characterized.

that which stays near the wall occurs in the range from six orifices per module to twelve orifices per module. The most uniformly mixed module at  $J=36$  (the ten hole module) has a jet penetration distance normalized by the module radius of 35 percent as measured from the module wall. The most uniformly mixed module at  $J=73$  (the fifteen hole module) has a jet penetration distance normalized by the module radius of 44 percent as measured from the module wall.



Table 5.3 Semi-Quantitative Jet Trajectory Characteristics For J=73 Round Hole Modules

Number of Orifices	Linear Penetration Depth (%)	% Mean Jet Penetration Depth @ $z/R=1$	Center Line Impingement
6	33	100	intersects
8	25	76	will intersect upstream of $z/R=1$
10	12	72	likely will intersect upstream of $z/R=1$
12	8	62	likely will not intersect upstream of $z/R=1$
15	5	44	will not intersect
18	3	24	definitely will not intersect

### 5.2.2 Mixing at One Duct Radius Downstream

From Figures 5.4 and 5.5, coupled with Table 5.3, one can obtain an intuitive feeling of the mixing process that is taking place in the module. However, more information is needed to select an optimum mixer. This issue is addressed in Figures 5.7 and 5.8.

A perfectly mixed plane of fluid would have a mixture fraction STD of zero. Figure 5.7 shows the mixture fraction STD as a function of distance normalized from the leading edge of the orifice ( $z/R = 0.0$ ) to one duct radius downstream ( $z/R = 1.0$ ) for the J=73 modules. The mixture uniformity as characterized by the STD values decreases as the number of orifices increases until the optimum number of orifices is reached and thereafter the value increases. As is suggested in Figure 5.4, the 15 orifice module yields the most uniform mixing. Figure 5.8 is the J=36 analogy to Figure 5.7. The trends are the same for both the J=36 and J=73 cases.

Figure 5.9 depicts the data from Figures 5.7 and 5.8 at the  $z/R=1.0$  plane. This figure clearly illustrates the STD minima that occurs at the optimal mixing configuration. Of the modules tested, the 15 orifice module was the best performer at J=73 and the 10 orifice module was the best performer at J=36.

The mean jet penetration depth at one mixer radius downstream of the leading edge of the orifices as a function of orifice number for the J=73 modules is shown in Figure 5.10. Note in this figure, that the best mixers, namely the 12, 15, and 18 orifice

modules, all display a penetration depth between 20% and 60% of the distance between the wall and the module's center line. Not coincidentally, the radius that divides the module's cross-section into an equal area circle and annulus, occurs at 30% of the distance from the wall (a "half area radius"). This suggests that the optimum mixer would likely be the one where the mean jet trajectory ended up on the "half area radius". At this penetration depth, the jet fluid would be exposed to equal amounts of mainstream material on either side of the jet.

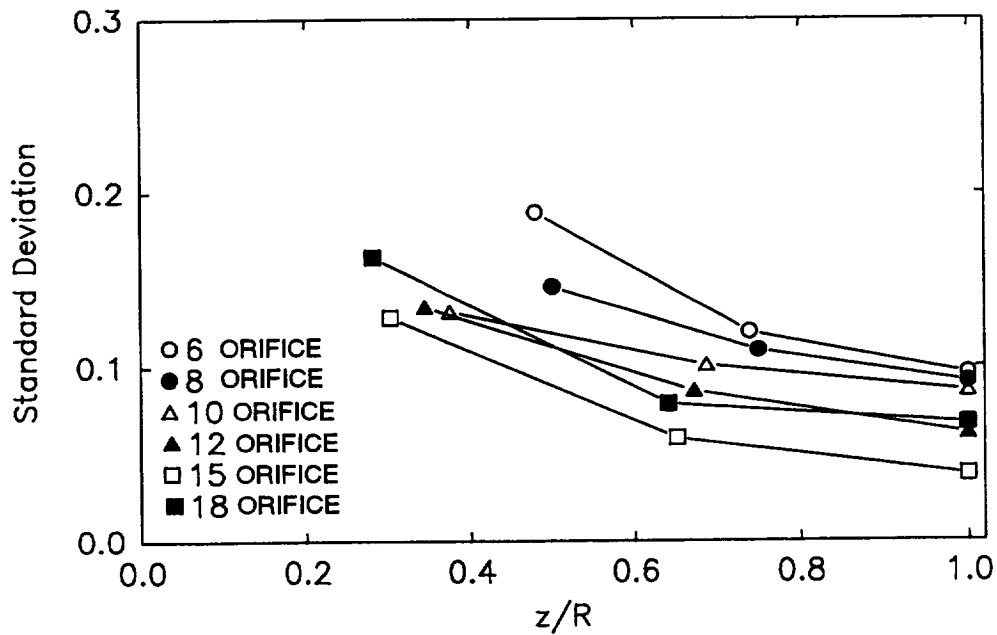


Figure 5.7 Area weighted standard deviation per plane for the  $J=73$  momentum-flux ratio modules (orifice leading edge @  $z/R=0.0$ , one duct radius downstream @  $z/R=1.0$ ).

These results agree with the relation proposed by Holdeman (1993) for optimal mixing in a can configuration, where the number of orifices ( $n$ ) is

$$n = \pi\sqrt{2J} / C$$

With  $C=2.5$ , as was reported to result in optimum one-side mixing in a rectangular geometry, fifteen orifices is predicted for  $J=73$ , and eleven orifices is predicted for  $J=36$ .

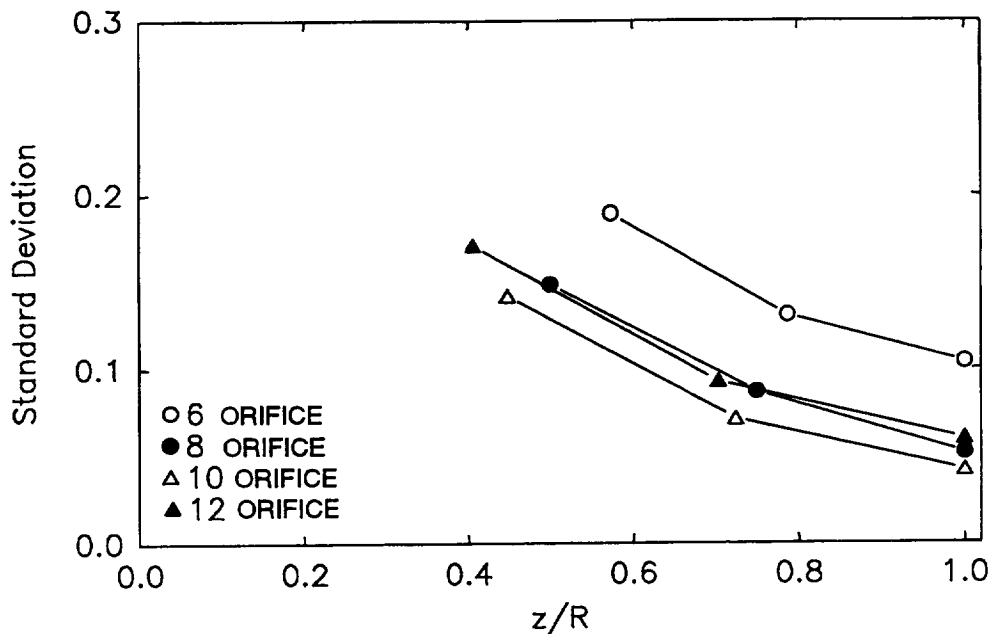


Figure 5.8 Area weighted standard deviation per plane for the  $J=36$  momentum-flux ratio modules (orifice leading edge @  $z/R=0.0$ , one duct radius downstream @  $z/R=1.0$ ).

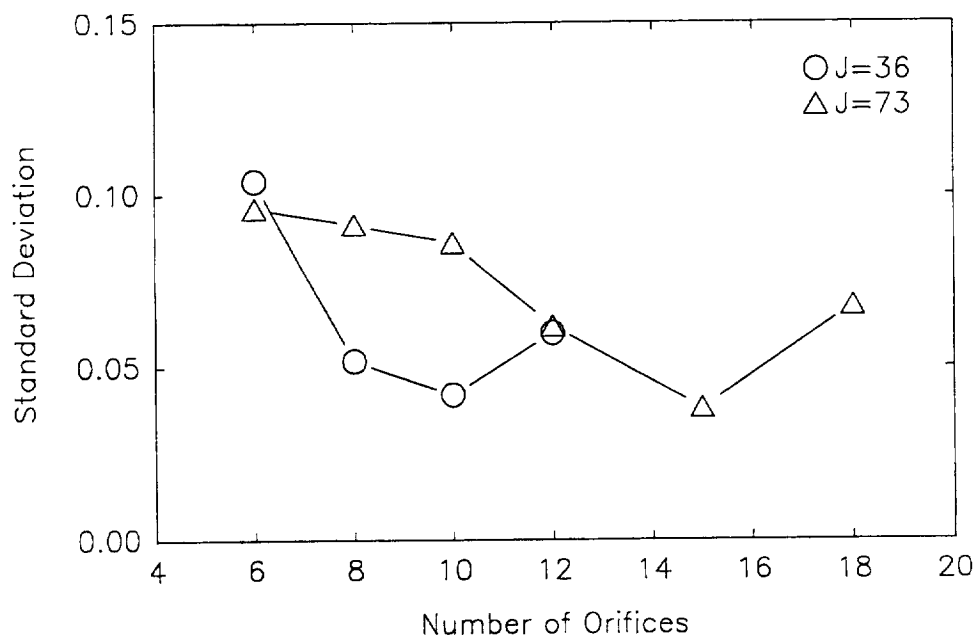


Figure 5.9 Area weighted standard deviation as a function of the number of orifices at @  $z/R=1.0$ .

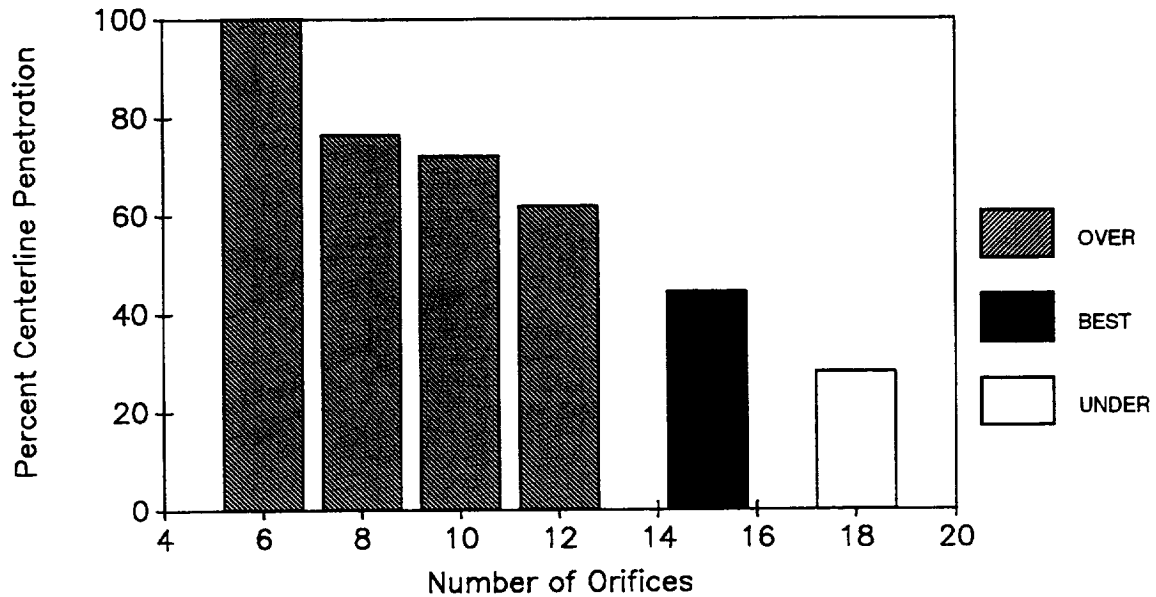


Figure 5.10 Mean jet trajectory penetration depth @  $z/R=1.0$  for the  $J=73$  momentum-flux ratio modules.

### 5.3 Global Orifice Optimization

The global optimization experiments encompassed the number of orifices, the orifice long-to-short side aspect ratio, and the orifice angle design parameters at a single momentum-flux ratio ( $J$ ) of 40 and mass flow ratio of 2.5 with the objective of uncovering the combination of the parameters that provides the best mixing possible. The momentum-flux ratio of 40 was selected as (1) a value close to but rounded up from the  $J=36$  value used in the circular orifice geometry experiments and (2), along with the mass flow ratio of 2.5, the most closely aligned to probable application in a practical system.

Table 5.4 lists the orifice axial height and the percentage of orifice blockage for the 13 mixing configurations considered. The orifice axial height is expressed as the ratio of the axial span of the orifice ( $h$ ) to the radius of the mixing module ( $R=1.5$  inches). The percent blockage is expressed as a ratio of the total circumferential span of the orifices to the circumference of the mixer. Both parameters are important in the design of orifices for optimal mixing.

The operating conditions are listed in Table 5.5.

Table 5.4 Normalized Orifice Axial Height and Percent Blockage

Number of Orifices	Orifice Aspect Ratio	Orifice Angle	h/R	Blockage (%)
16	5	30	0.62	41
16	3	0	0.55	47
16	3	60	0.37	94
16	1	30	0.34	88
12	5	0	0.81	31
12	5	60	0.48	62
12	3	30	0.58	47
12	1	0	0.40	76
12	1	60	0.40	76
8	5	30	0.88	29
8	3	0	0.78	33
8	3	60	0.52	67
8	1	30	0.49	62

Table 5.5 Global Optimization Operating Conditions

T <sub>main</sub> (°F)	T <sub>jet</sub> (°F)	P (psia)	V <sub>main</sub> (ft/s)	M <sub>main</sub> (lbm/s)	Mass-flow Ratio	Density Ratio
212	74	14.7	31.0	0.090	2.5	1.28

The normalized orifice axial height ( $h/R$ ) corresponds to the axial rate of jet mass addition. To illustrate its importance to mixing, consider two extreme cases;  $d/R=1.0$  and  $d/R=0.0$ . For the case where  $d/R=1.0$ , the jet fluid addition process is continuing right up to the final mixing analysis plane at  $z/R=1.0$ . The jet fluid that passes through the top of the orifice does not have the opportunity to mix with the main fluid. This results in hot and cold spots in the analysis plane and a correspondingly high mixture fraction standard deviation.

At the other extreme is the case where  $d/R=0.0$ . This corresponds to the jet fluid being added instantaneously, thereby having the entire residence time between  $z/R=0.0$  and  $z/R=1.0$  to mix with the main fluid.

The percentage of orifice blockage for a given orifice long-to-short side aspect ratio and number of orifices is inversely proportional to the orifice axial height. A high aspect ratio design (long and narrow) at a zero degree orifice inclination angle (aligned with the mixer's center-line) would have a large  $d/R$  and a small percentage of orifice blockage. The opposite is also true.

As the percentage of orifice blockage approaches 100, the jet flow approaches the point of completely inhibiting the flow of the main fluid near the module's wall. This can have the advantage of cooling the walls at the expense of allowing an undiluted core of main fluid to pass through the mixer section. Similarly, with an orifice angle of zero (i.e., no orifice induced swirl component), as the percentage of orifice blockage approaches zero the jet penetration would be great and a large portion of the walls would be exposed to undiluted main fluid while the jets impinged upon one-another at the module's centerline.

Slotted orifice designs at non-zero orifice angles act as swirl vanes to the approaching main-flow. In the consideration of jet penetration, the swirl component imparted on the main-flow must be considered.

### **5.3.1 Mixture Fraction Contours at $z/R=1.0$**

The diagrammatic view of the test matrix design space has been included in Figure 5.11 to familiarize the reader with the particular parameter combinations that were experimentally considered. Each of the thirteen orifice arrangements that were manufactured and tested is represented by a solid black point. The mixture fraction contour plots in Figures 5.13, 5.15, and 5.17 are arranged in the same relative positions as the design points for the 16, 12, and 8 orifice design planes, respectively. Figures 5.12, 5.14, and 5.16 represent design cube slices for the 16, 12, and 8 orifice planes, respectively.

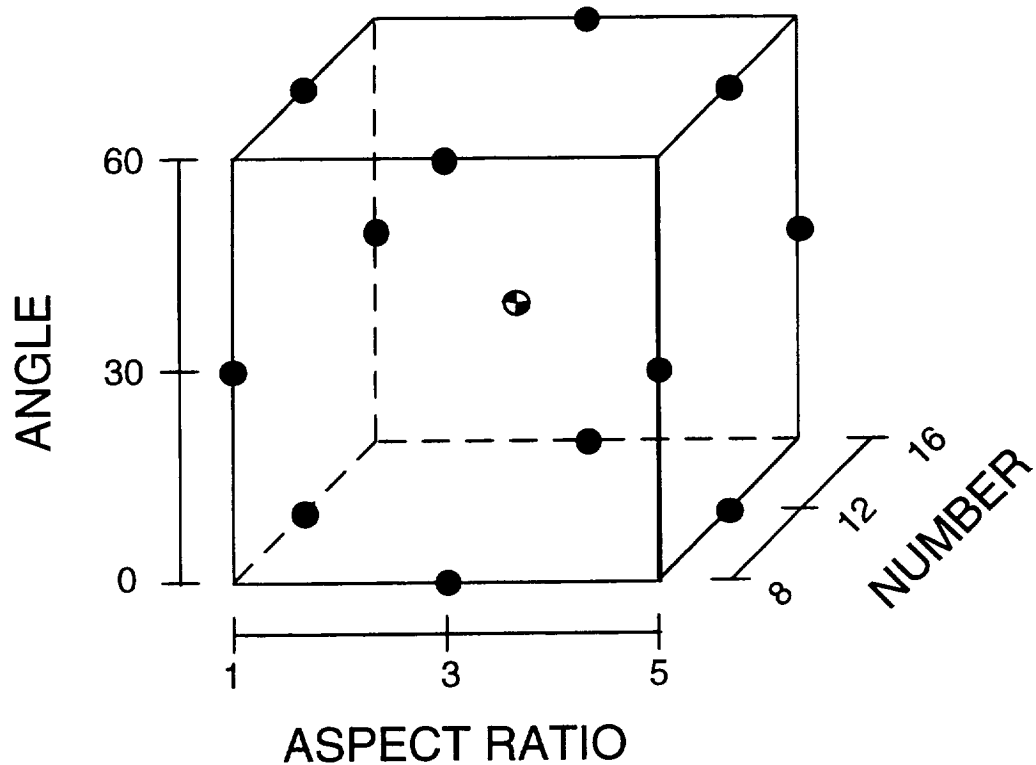


Figure 5.11 Graphical representation of test matrix

Figures 5.13, 5.15, and 5.17 are mixture fraction contour plots at the  $z/R=1.0$  axial plane. Each contour slice is labeled with a numerical designator of the form number/aspect ratio/angle. For example, 16/3/30 signifies the 16 orifice module at a long-to-short side aspect ratio of 3 and an orifice angle of 30 degrees from the module's centerline. These figures are useful for making a relative visual comparison between the flow field uniformity of one mixer versus another.

Figure 5.13 depicts the mixture fraction contours for all four of the 16 orifice modules that were examined. Recall that the mixture fraction is calculated directly from the measured temperature at each measurement point from the following relationship:

$$f = \frac{T_{mixed} - T_{jet}}{T_{main} - T_{jet}}$$

Accordingly, the red colors ( $f > 0.8$ ) correspond to a hot region in the flow field where the main fluid is predominate. Likewise, the blue colors ( $f < 0.2$ ) correspond to a cold region in the flow field where the jet fluid is predominate.

Each of the contours in Figure 5.13 contains several mixture fraction contours indicating relatively poor mixing. Each of the configurations suffers from under-penetration of the jet fluid. This is obvious from the high thermal stratification between the cold walls and the hot center-line. The combination of the 94% blockage of the 16/3/60 mixer, the highest of any mixer in the test matrix, and the strong swirl component that arises from the 60 degree inclination of the 3:1 long-to-short side aspect ratio slots, gives this mixer the highest thermal stratification and the highest mixture fraction standard deviation (STD) of 0.165. The 16/1/30 mixer, despite the absence of any swirl component due to the round hole orifices (1:1 long-to-short side aspect ratio), comes in a close second for the worst mixer with an 88% blockage and a STD of 0.155.

Within the 16 orifice design plane, the 16/3/0 and the 16/5/30 mixers perform relatively well, but pale in comparison to the advantages that can be gained by reducing the number of orifices to 12.

With the exception of the 12/5/60 configuration, each of the 12 orifice modules in Figure 5.15 show just two mixture fraction contours. As expected, the 12/5/60 configuration has the worst STD of the 12 orifice group. This is due to the combination of the high percentage of blockage and the high swirl component that is imparted on the main flow due to the high long-to-short side aspect ratio and the high orifice angle. These two factors combine to dilute the jet strength to the point where the jet presence at the center-line is minimal.

The contour plots for the 12/1/60 and 12/1/0 mixers are identical because the mixers are one-in-the-same. This is explained by the fact that at the limit where the long-to-short side aspect ratio is unity, the orifice is circular. The symmetry of the circular orifice makes it insensitive to the inclination angle.



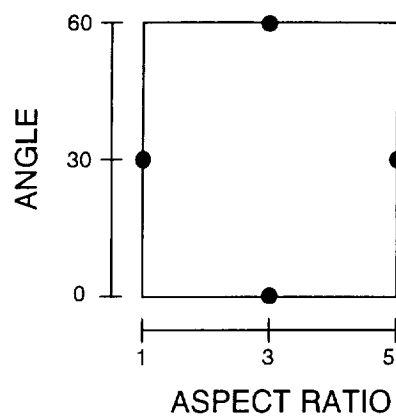


Figure 5.12 Sixteen orifice modules' design plane

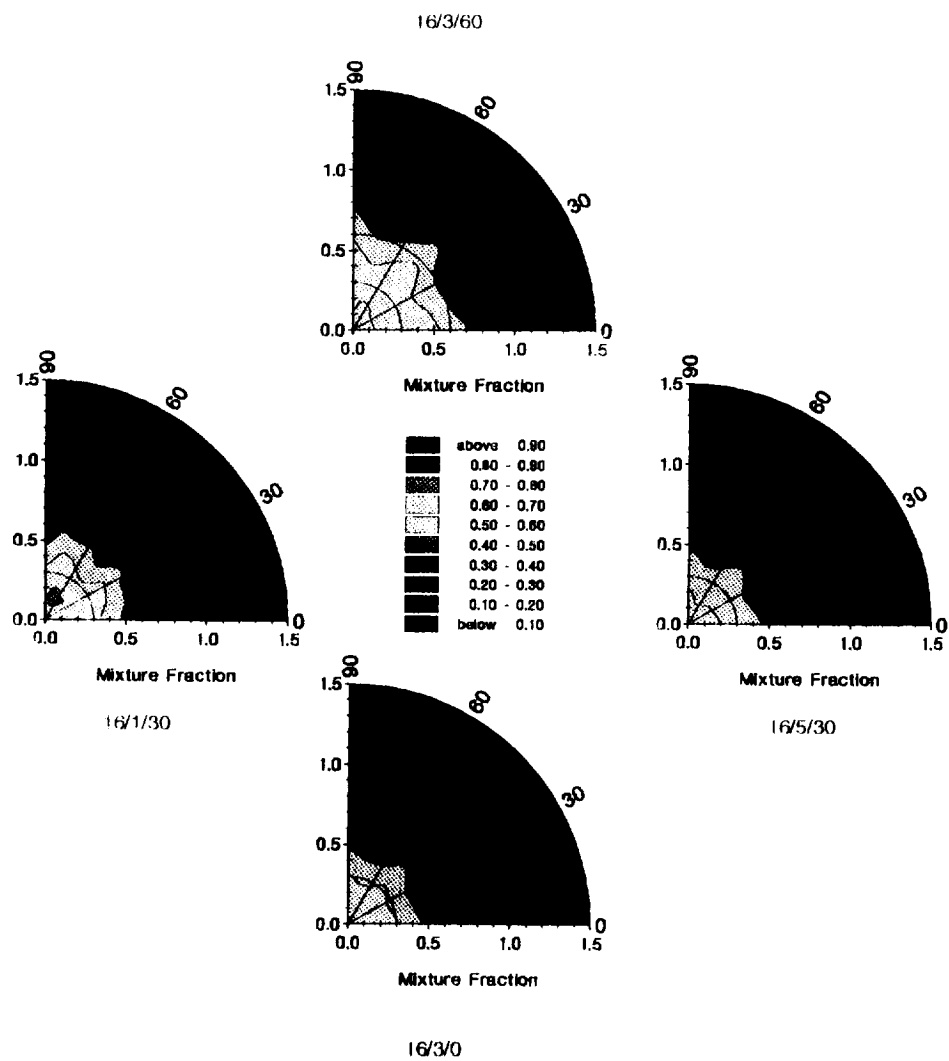


Figure 5.13 Sixteen orifice modules' mixture fraction contours at  $z/R=1.0$

In considering the 12 orifice configurations, the best evidence that mixing performance can be enhanced by reducing the number of orifices from 16 to 12 is provided by the fact that the 12/5/0 configuration is the best mixer of the group with the lowest percentage of blockage and no orifice angle induced swirl.

As a whole, the 8 orifice design plane mixers are the best performers considered. Each plot is dominated by a single mixture fraction contour, with relatively small areas of the other contours. Two extremes in jet penetration are illustrated by the 8/3/60 and the 8/3/0 configurations. Of the four different 8 orifices modules, these two are the worst mixers, but for different reasons. The 8/3/60 configuration has both a high percentage of blockage (67%) and an orifice induced swirl component giving it a cold wall and a hot center-line. The 8/3/0 module has a well-mixed center-line and hot spots along the wall. This is due to the low percentage of blockage (33%) and the absence of any orifice induced swirl component.

The narrow orifices of the 8/5/30 configuration combine with the 30 degree orifice angle to strike a balance between blockage, jet penetration, and swirl. Of all 13 arrangements tested, the 8/5/30 mixer yields the best mixed plane of fluid at  $z/R=1.0$ .

The mixture fraction standard deviation (STD) results of these experiments are shown in Figure 5.18. These values are the average results of the original and repeat experiments at the  $z/R=1.0$  plane.

The average mixture fraction standard deviation values as shown in Table 5.6 reveal that the degree of mixedness is improved for the experiments conducted at a jet-to-main stream momentum-flux ratio of 40 by reducing the number of orifices from 16 to 8. As a note, this trend may not hold when additional mixer configurations are added to the test matrix. Evidence of this is shown in Figure 5.12 in Section 5.2.2. This figure shows that the 10 circular orifice mixer at a jet-to-main stream momentum-flux ratio of 36 and a mass-ratio of 2.2, out-performed any of the configurations in the “Global Optimization” test matrix.

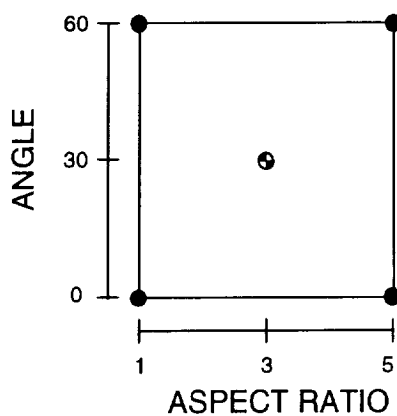


Figure 5.14 Twelve orifice modules' design plane

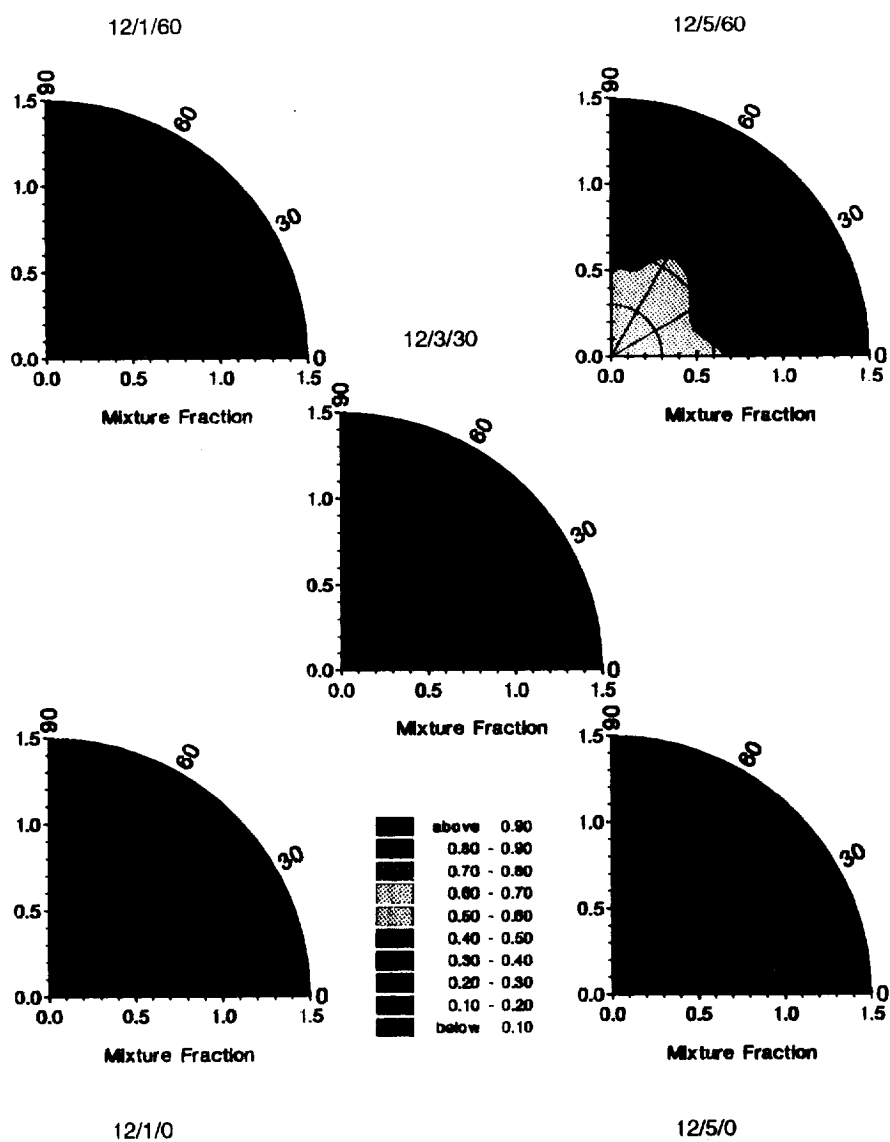


Figure 5.15 Twelve orifice modules' mixture fraction contours at  $z/R=1.0$

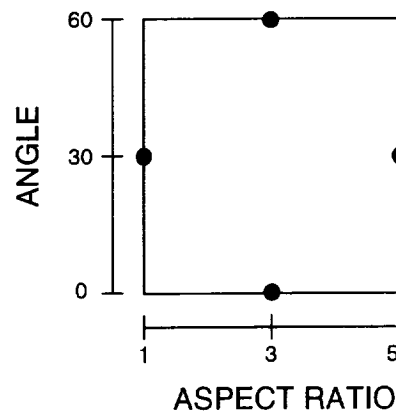


Figure 5.16 Eight orifice modules' design plane

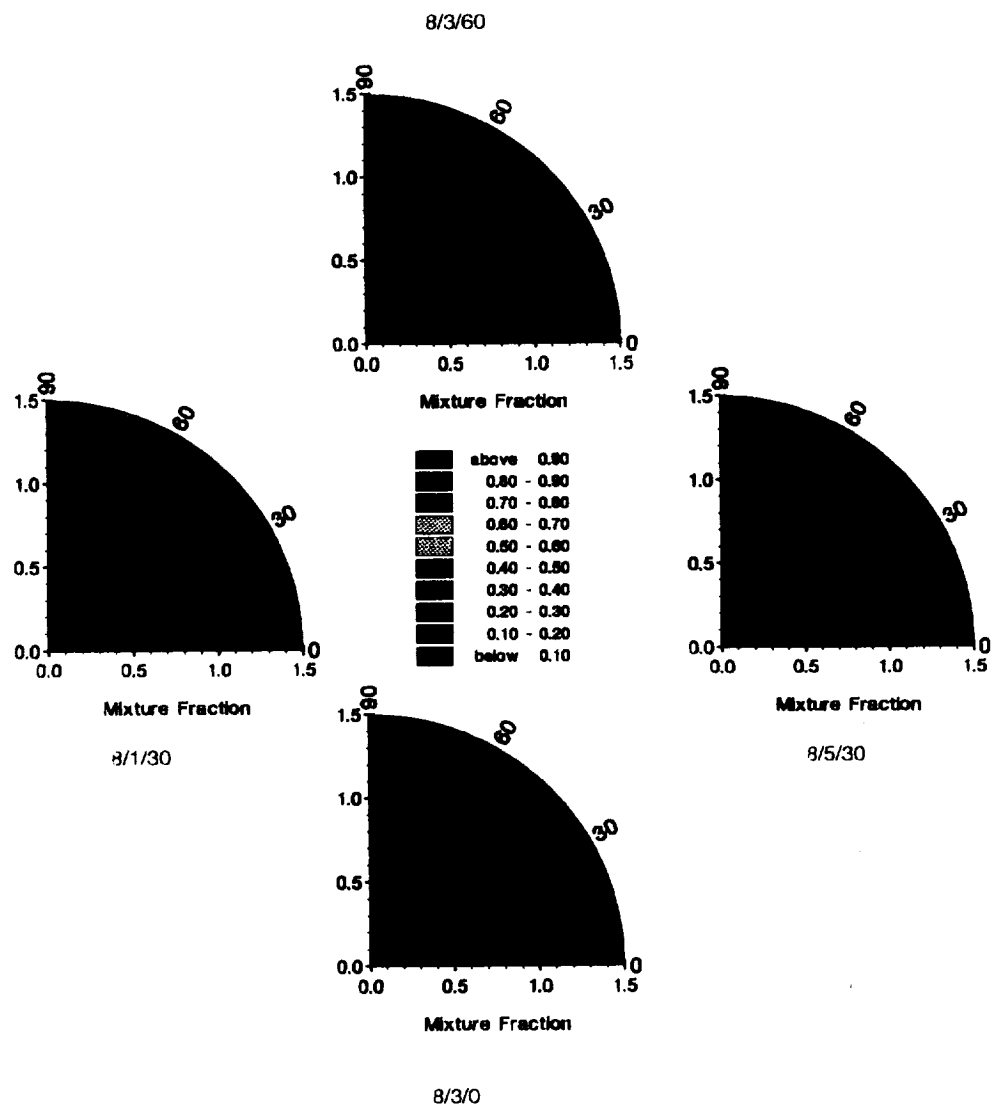


Figure 5.17 Eight orifice modules' mixture fraction contours at  $z/R=1.0$

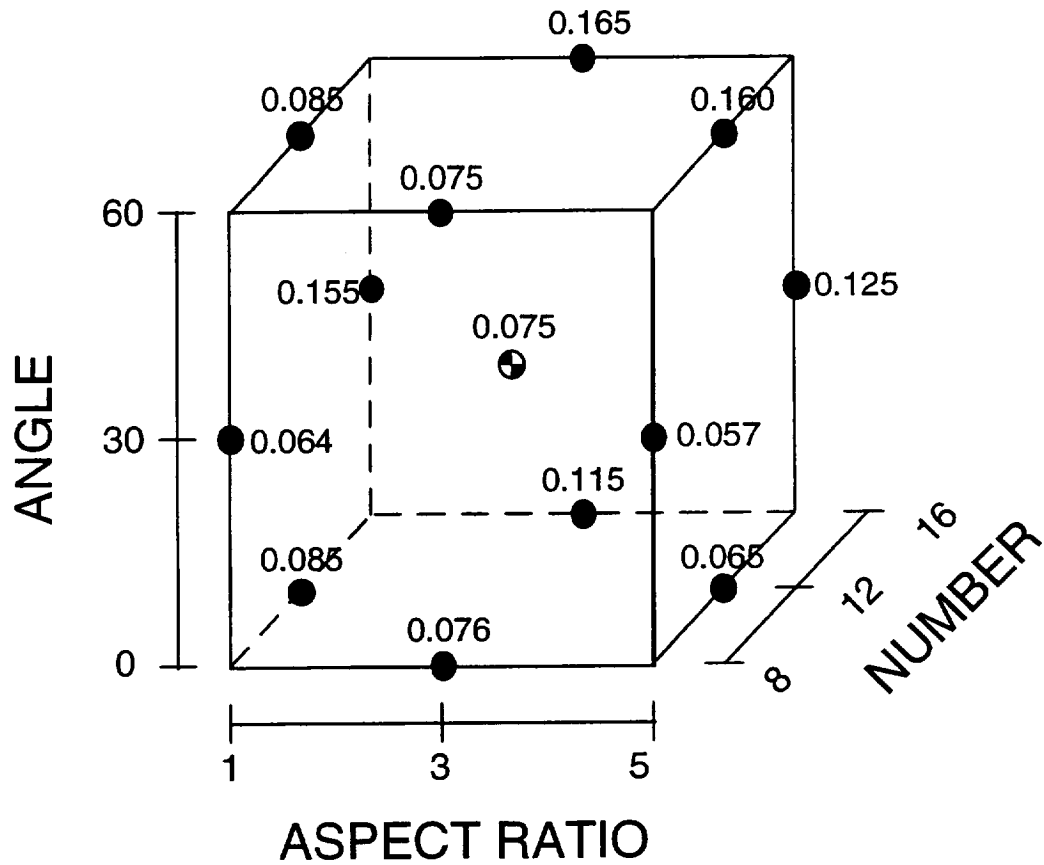


Figure 5.18 STD results as a function of the orifice design parameters at  $z/R=1.0$

Table 5.6 Average Mixture Fraction STD values at  $z/R=1.0$

Orifice Plane	Average STD
16	0.140
12	0.118
8	0.068

The mean-jet penetration depth at one mixer radius downstream of the leading edge of the orifices ( $z/R=1.0$ ) is a primary parameter for the optimization of mixing. The experiments showed that mixing performance is strongly correlated with the jet penetration, with the best mixers having a penetration depth at  $z/R=1.0$  of roughly one-half of the mixing duct radius. These penetration results are shown pictorially as a function of the three design parameters in Figure 5.19. The three dimensional design

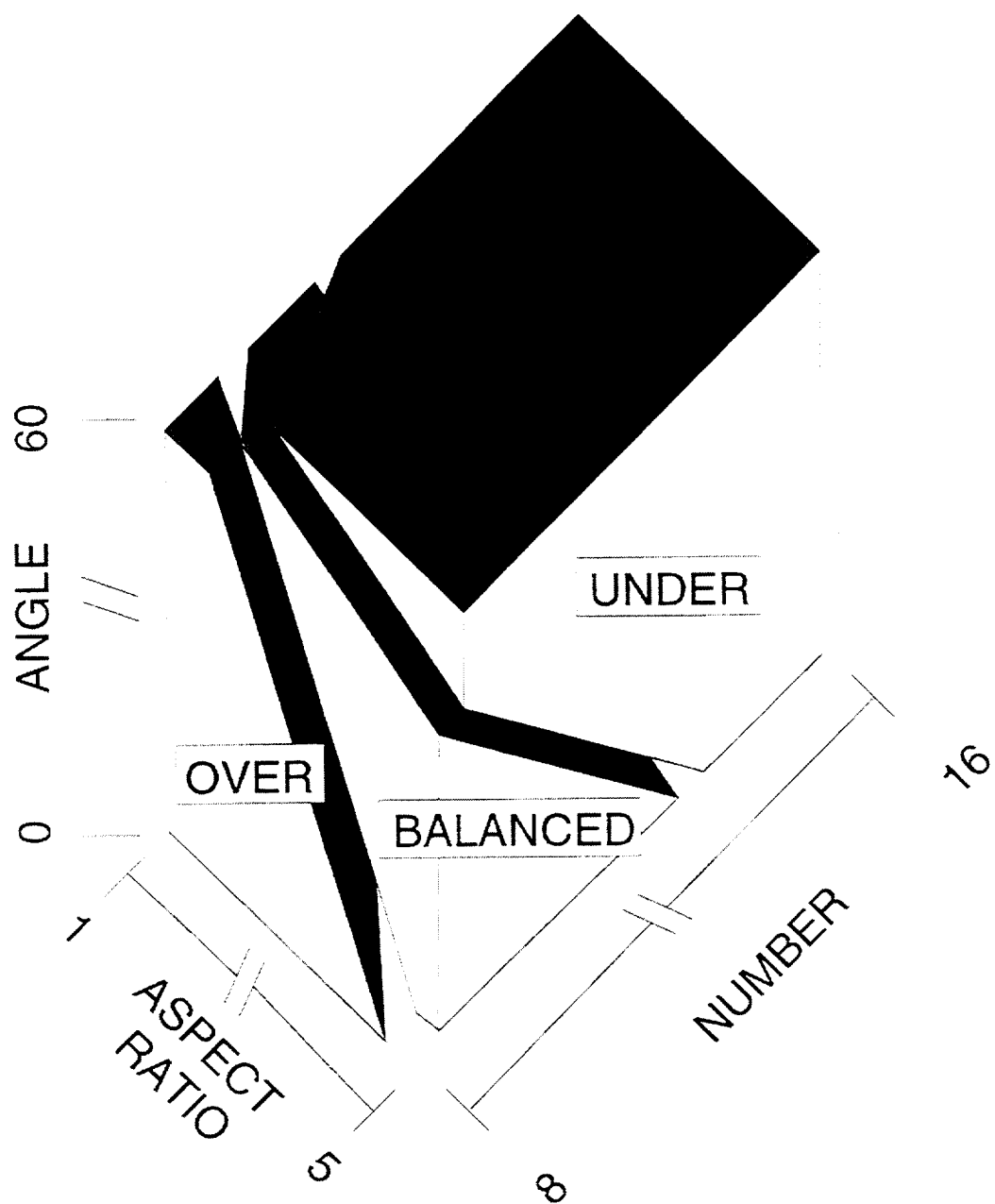


Figure 5.19 Mean Jet Penetration results at  $z/R=1.0$  as a function of the orifice design parameters.

space has been partitioned into three sectors representing over, under, and balanced jet penetration. This figure hints at the complexities involved in trying to select the optimal combination of the three orifice design parameters.

### 5.3.2 Linear Regression Analysis

A linear regression was performed on the 26 data points arising from the 13 original and the 13 repeat experiments using the Rummage II (1987) statistical analysis software. The following interpolating equation was arrived at for the STD as a function of the three experimental parameters; i.e., the number of orifices ( $n$ ), the orifice long-to-short side aspect ratio ( $AR$ ), and the orifice angle ( $\alpha$ ). Insignificant terms were eliminated from the model using conventional statistical methods.

$$\text{STD} = C_1 * n + C_2 * n^2 + C_3 * AR * \alpha + C_4 * n^2 * AR + C_5 * AR^2 * \alpha + C_6 * AR * \alpha^2 + C_7 * n * AR * \alpha + C_8$$

where:

$$\begin{aligned} C_1 &= -0.019999 \\ C_2 &= 0.001301 \\ C_3 &= -0.000845 \\ C_4 &= -0.000057 \\ C_5 &= 0.000090 \\ C_6 &= 0.000007 \\ C_7 &= 0.000025 \\ C_8 &= 0.152869 \end{aligned}$$

The OPTDES.BYU optimization program (Parkinson, Balling, and Free, 1988) was used to locate the minima of the STD interpolating equation. Several iterations of the code were executed to distinguish the multiple local minima from the single global minima. This procedure yielded the following values for the orifice design parameters and the STD:

$$\begin{aligned} n &= 8.23 \\ AR &= 3.66 \\ \alpha &= 22.16 \\ \text{STD} &= 0.04972 \end{aligned}$$

By constraining the program to considering only integer values of the number of orifices, the following values were obtained:

$$\begin{aligned}n &= 8.00 \\AR &= 3.55 \\\alpha &= 23.24 \\STD &= 0.04976\end{aligned}$$

The limitation of the STD interpolating equation is evident by comparing the STD of the predicted optimal configuration to the STD values for the circular orifice mixers that have been plotted in section 5.2.2, Figure 5.9. This figure shows that the best circular orifice configuration tested at  $J=36$  was the ten orifice mixer, resulting in an STD value of 0.042. The performance of the 10 circular orifice mixer (long-to-short side aspect ratio of one) indicates that the global optimization test matrix is missing some vital information within the design space range of the optimal configuration, despite the slight difference in the momentum-flux ratios and the mass-ratios of the two sets of experiments.

In as much as this model is highly biased with the under-penetrating cases, another test matrix closer to the optimum mixer configuration needs to be run before an optimum configuration can be identified. This is true because of the highly non-linear relationship between the STD and the orifice design parameters as seen in the above equation.



## CHAPTER 6

### CONCLUSIONS AND RECOMMENDATIONS

#### 6.1 Conclusions

As a result of the thermocouple probe perturbation investigation, the following conclusions were established:

- The probe design can influence the flow field.
- Modifying the probe design affects the degree and severity of back-flow in the vicinity of the orifices.
- A 45 degree probe provides the least amount of flow field disturbance of the three probe types that were considered.

The orifice optimization experiments revealed the following conclusions:

- Mixture uniformity is a non-linear function of the number of orifices, the orifice long-to-short side aspect ratio, and the orifice angle.
- Jet penetration depth is a function of circumferential blockage, axial jet mass addition rate, and orifice induced swirl.
- For a fixed orifice aspect ratio and angle, higher momentum-flux ratios optimize at higher numbers of orifices.
- Optimum mixing occurs when the asymptotic mean jet trajectories are in the range of  $0.35 < r/R < 0.5$ .

## 6.2 Recommendations

For the study as a whole:

- The thermocouple temperature measurement system could be improved upon with a digital planar imaging system such as the Mie-scattering arrangement used by Liscinsky et al. (1992).

The optimization analysis can benefit from the following steps:

- Manufacture and test the nine additional mixers specified in Table 6.1 to complement the current global optimization test matrix in the vicinity of the optimal configuration.

Table 6.1 Additional Global Optimization Experiments

Number	Aspect Ratio	Angle
6	3	0
6	3	60
6	5	30
8	3	30
8	5	0
8	5	60
10	3	0
10	3	60
10	5	30

- Perform another linear regression on the combined results of the thirteen original and the nine additional experiments to arrive at a higher resolution interpolating equation.
- Use an optimization algorithm to arrive at the optimal orifice geometry combination from the new interpolating equation.
- Manufacture and test the predicted optimal configuration and compare it against its expected performance.

## CHAPTER 7

### REFERENCES

- Bain, D.B., Smith, C.E., and Holdeman, J.D. "CFD Mixing Analysis of Jets Injected from Straight and Slanted Slots into Confined Crossflow in Rectangular Ducts," AIAA 92-3087, 1992. (also NASA TM 105699).
- Bain, D.B., Smith, C.E., and Holdeman, J.D. "CFD Mixing Analysis of Axially Opposed Rows of Jets Injected into Confined Crossflow," AIAA 93-2044, 1993. (also NASA TM 106179).
- Bruce, T.W., Mongia, H.C., and Reynolds, R.S. "Combustor Design Criteria Validation," AiResearch Manufacturing Co., Phoenix, AZ, AiResearch 75-211682(38)-1, March 1979. (USARTL-TR-78-55A).
- Fletcher, R.S., "Emissions," *The Design and Development of Gas Turbine Combustors*, Vol. 1, Northern Research and Engineering Corporation, Woburn, Massachusetts, pp. 7.1-7.110, 1980.
- Glassman, I., *Combustion*, Second Edition, Academic Press, Orlando, 1987.
- Hatch, M.S., Sowa, W.A., Samuelson, G.S., and Holdeman, J.D., "Jet Mixing Into a Heated Cross Flow in a Cylindrical Duct: Influence of Geometry and Flow Variations," AIAA-92-0773, 1992. (also NASA TM 105390).
- Holdeman, J. D., "Mixing of Multiple Jets with a Confined Subsonic Crossflow," Prog. Energy Combust. Sci., **19**, pp. 31-70, 1993 (also AIAA-91-2458 and NASA TM 104412).
- Holdeman, J.D., Srinivasan, R., Reynolds, R., and White, C.D. "Studies of the Effects of Curvature on Dilution Jet Mixing," J. of Propulsion and Power, Vol. 7, no. 4, Jul-Aug 1991.
- Howe, G.W., Li, Z., Shih, T.I.-P., and Nguyen, H.L., "Simulation of Mixing in the Quick Quench Region of a Rich Burn-Quick Quench Mix-Lean Burn Combustor," AIAA 91-0410, 1991.
- Johnston, H., 1971, "Reduction of Stratospheric Ozone by Nitrogen Oxide Catalysts from Supersonic Transport Exhaust," *Science*, Vol. 173, pp. 517-521.
- Kandebo, S.W. "HSCT Propulsion Studies Focus on Reducing Emissions, Noise," Aviation Week & Space Technology, July 10, 1989.
- Kandebo, S.W. "NASA-Industry Propulsion Team Addressing HSCT Environmental Issues," Aviation Week & Space Technology, November 25, 1991.
- Kandebo, S.W. "HSCT Propulsion Team Mulls Flight Test Issue," Aviation Week & Space Technology, August 31, 1992.
- Kuo, K.K., *Principles of Combustion*, John Wiley & Sons, New York, 1986.

- Lefebvre, A.H., *Gas Turbine Combustion*, Hemisphere Publishing Corporation, Washington, 1983.
- Liscinsky, D.S., True, B., Vranos, A., and Holdeman, J. D., "Experimental Study of Cross-Stream Mixing in a Rectangular Duct," AIAA-92-3090, 1992. (also NASA TM 105694).
- Liscinsky, D.S., True, B., and Holdeman, J. D., "Experimental Investigation of Crossflow Jet Mixing in a Rectangular Duct," AIAA-93-2037, 1993. (also NASA TM 106152).
- Mosier, S.A. et al., "Advanced Combustor Systems for Stationary Gas Turbines," U.S. Environmental Protection Agency, Final Report FR 11405, Contract 68-02-2136, March 31, 1980.
- Nakata, T. et al., "Design and Test of a Low-NO<sub>x</sub> Advanced Rich-Lean Combustor for LBG Fueled 1300°C-Class Gas Turbine," ASME 92-GT-23, 1992.
- Noyce, J.R., Sheppard, C.G.W., and Yamba, F.D., "Measurements of Mixing and Species Concentrations within a Gas Turbine Type Combustor," *Combustion Science and Technology*, Vol. 25, pp. 209-217, 1981.
- Oechsle, V.L., Mongia, H.C., and Holdeman, J. D., "A Parametric Numerical Study of Mixing in a Cylindrical Duct," AIAA-92-3088, 1992. (also NASA TM 105695).
- Oechsle, V.L., Mongia, H.C., and Holdeman, J. D., "An Analytical Study of Jet Mixing in a Cylindrical Duct," AIAA-93-2043, 1993. (also NASA TM 105695).
- Ott, J. "Contractors Urge Further Research to Validate HSCT Technologies," *Aviation Week & Space Technology*, October 17, 1988.
- Parkinson, A., Balling, R., and Free, J., OPTDES.BYU Release 4.0, Departments of Mechanical and Civil Engineering, Brigham Young University, Provo, UT, 1988.
- Peters, J.E. and Hammond Jr., D.C., "Introduction to combustion for gas turbines," *Design of Modern Turbine Combustors*, Academic Press Inc., San Diego, CA, 1990.
- Rizk, N.K., and Mongia, H.C., "Rich-lean combustor gives very lean NO<sub>x</sub>," *Modern Power Systems*, Vol. 10, No. 9, pp. 83-85, Sept. 1990.
- Scott, D.T., Carter, M.W., and Bryce, G.R., RUMMAGE II, Statistics Department, Brigham Young University, Provo, UT, 1987.
- Shaw, R.J., "Engine Technology Challenges for a 21st Century High Speed Civil Transport," AIAA Tenth International Symposium on Air Breathing Engines, September 1-6, 1991 (also NASA TM 104363).
- Smith, C.E., "Mixing Characteristics of Dilution Jets in Small Gas Turbine Combustors," AIAA-90-2728, 1990.
- Smith, C.E., Talpallikar, M.V., and Holdeman, J.D. "Jet Mixing in Reduced Areas for Lower Combustor Emissions in Gas Turbine Combustors," AIAA 91-2460, 1991. (also NASA TM 104411).

Smoot, L.D., and Smith, P.J., *Coal Combustion and Gasification*, Plenum Press, New York, 1985.

Strack, W.C., and Morris, S.J., "The Challenges and Opportunities of Supersonic Transport Propulsion Technology," AIAA 88-2985, 1988.

Tacina, R.R., "Low NO<sub>x</sub> Potential of Gas Turbine Engines," AIAA-90-0550, 1990.

Talpallikar, M.V., Smith, C.E., Lai, M.C., and Holdeman, J.D. "CFD Analysis of Jet Mixing in Low NO<sub>x</sub> Flametube Combustors," AIAA 91-217, 1991. (also NASA TM 104466).

Vranos, A., Liscinsky, D., True, B., and Holdeman, J.D. "Experimental Study of Cross-Stream Mixing in a RQL Combustor Quench Section Model," AIAA 91-2459, 1991. (also NASA TM 105180).

Zeldovich, J., 1946, "The Oxidation of Nitrogen in Combustion and Explosions," *Acta Physicochimica*, URSS, Vol. 21, 4, pp. 577-628.

## APPENDIX A

### DERIVATION OF PERCENTAGE OF JET MASS ADDED EQUATION

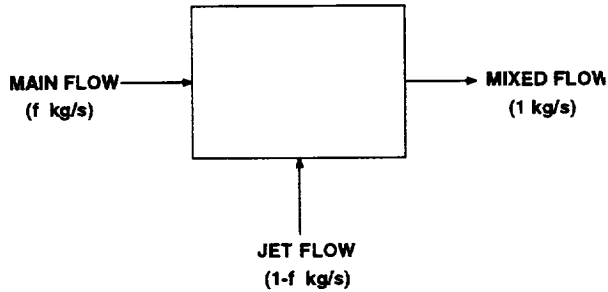
The motivation behind this derivation is to determine the percentage of the total jet flow mass that has been accounted for at a given axial plane based on the available mixture fraction values.

Start with the equation:  $\% \text{ jet mass added} = 100 * \left( \frac{m_{jet}^i}{m_{jet}^f} \right)$  equation (1)

where:  $m_{jet}^i$  = jet mass existing at plane i

$m_{jet}^f$  = total (final) amount of jet mass

In an effort to express the masses in terms of the mixture fraction, consider the derivation of the mixture fraction, f:



Any conserved scalar z can be expressed in terms of the mixture fraction.

$$z_{mixed} = z_{main}f + z_{jet}(1 - f)$$

Solving for the mixture fraction yields:

$$f = \frac{z_{mixed} - z_{jet}}{z_{main} - z_{jet}}$$

The temperature is the conserved scalar used in the RQL mixing experiments (since no reactions are occurring), giving a mixture fraction defined as:

$$f = \frac{T_{mixed} - T_{jet}}{T_{main} - T_{jet}}$$

To express the % jet mass added equation in terms of the mixture fraction, consider the following definition of mixture fraction.

$$f = \frac{m_{main}}{m_{main} + m_{jet}} = \frac{f}{f + (1 - f)} = f$$

Define:  $\bar{f}^i$  as the average mixture fraction for plane i

$f_{eq}$  as the equilibrium mixture fraction after all jet mass has been added

Note that:  $\bar{f}^i = f_{eq}$  after the completion of the mass addition process

then:

$$\bar{f}^i = \frac{m_{main}}{m_{main} + m_{jet}^i}$$

yielding:

$$m_{jet}^i = m_{main} \left( \frac{1}{\bar{f}^i} - 1 \right) \quad \text{equation (2)}$$

similarly:

$$f_{eq} = \frac{m_{main}}{m_{main} + m_{jet}^f}$$

yielding:

$$m_{jet}^f = m_{main} \left( \frac{1}{f_{eq}} - 1 \right) \quad \text{equation (3)}$$

Substituting equations (2) and (3) into equation (1) yields the desired relationship:

$$\% \text{ jet mass added} = 100 * \frac{f_{eq}}{\bar{f}^i} * \frac{1 - \bar{f}^i}{1 - f_{eq}}$$

REPORT DOCUMENTATION PAGE			Form Approved OMB No. 0704-0188	
Public reporting burden for this collection of information is estimated to average 1 hour per response, including the time for reviewing instructions, searching existing data sources, gathering and maintaining the data needed, and completing and reviewing the collection of information. Send comments regarding this burden estimate or any other aspect of this collection of information, including suggestions for reducing this burden, to Washington Headquarters Services, Directorate for Information Operations and Reports, 1215 Jefferson Davis Highway, Suite 1204, Arlington, VA 22202-4302, and to the Office of Management and Budget, Paperwork Reduction Project (0704-0188), Washington, DC 20503.				
1. AGENCY USE ONLY (Leave blank)		2. REPORT DATE April 1996		3. REPORT TYPE AND DATES COVERED Final Contractor Report
4. TITLE AND SUBTITLE  Optimization of Orifice Geometry for Cross-Flow Mixing in a Cylindrical Duct			5. FUNDING NUMBERS  WU-537-02-20 G-NAG3-1110	
6. AUTHOR(S)  J.T. Kroll, W.A. Sowa, and G.S. Samuelson				
7. PERFORMING ORGANIZATION NAME(S) AND ADDRESS(ES)  University of California Irvine, California 92717-3550			8. PERFORMING ORGANIZATION REPORT NUMBER  E-10247	
9. SPONSORING/MONITORING AGENCY NAME(S) AND ADDRESS(ES)  National Aeronautics and Space Administration Lewis Research Center Cleveland, Ohio 44135-3191			10. SPONSORING/MONITORING AGENCY REPORT NUMBER  NASA CR-198482 UCICL-ARTR-93-4	
11. SUPPLEMENTARY NOTES  Project Manager, J.D. Holdeman, Internal Fluid Mechanics Division, NASA Lewis Research Center, organization code 2650, (216) 433-5846.				
12a. DISTRIBUTION/AVAILABILITY STATEMENT  Unclassified - Unlimited Subject Category 07  This publication is available from the NASA Center for AeroSpace Information, (301) 621-0390.			12b. DISTRIBUTION CODE	
13. ABSTRACT (Maximum 200 words)  Mixing of gaseous jets in a cross-flow has significant applications in engineering, one example of which is the dilution zone of a gas turbine combustor. Despite years of study, the design of the jet injection in combustors is largely based on practical experience. The emergence of NO <sub>x</sub> regulations for stationary gas turbines and the anticipation of aero-engine regulations requires an improved understanding of jet mixing as new combustor concepts are introduced. For example, the success of the staged combustor to reduce the emission of NO <sub>x</sub> is almost entirely dependent upon the rapid and complete dilution of the rich zone products within the mixing section. It is these mixing challenges to which the present study is directed. A series of experiments was undertaken to delineate the optimal mixer orifice geometry. A cross-flow to core-flow momentum-flux ratio of 40 and a mass flow ratio of 2.5 were selected as representative of a conventional design. An experimental test matrix was designed around three variables: the number of orifices, the orifice length-to-width ratio, and the orifice angle. A regression analysis was performed on the data to arrive at an interpolating equation that predicted the mixing performance of orifice geometry combinations within the range of the test matrix parameters. Results indicate that the best mixing orifice geometry tested involves eight orifices with a long-to-short side aspect ratio of 3.5 at a twenty-three degree inclination from the center-line of the mixing section.				
14. SUBJECT TERMS  Dilution; Jet mixing flow; Gas turbine; Combustion chamber; Emissions			15. NUMBER OF PAGES 78	
			16. PRICE CODE A05	
17. SECURITY CLASSIFICATION OF REPORT Unclassified	18. SECURITY CLASSIFICATION OF THIS PAGE Unclassified	19. SECURITY CLASSIFICATION OF ABSTRACT Unclassified	20. LIMITATION OF ABSTRACT	





**National Aeronautics and  
Space Administration**

**Lewis Research Center**  
21000 Brookpark Rd.  
Cleveland, OH 44135-3191

Official Business  
Penalty for Private Use \$300

POSTMASTER: If Undeliverable — Do Not Return